Research Square

Preprints are preliminary reports that have not undergone peer review.
They should not be considered conclusive, used to inform clinical practice,
or referenced by the media as validated information.

Machine Learning Assisted Creep Deformation Time Prediction and Failure Analysis of 316L Stainless Steel at Elevated Temperatures

Arun Kumar

arunkumarbit326@gmail.com

CSIR-National Metallurgical Laboratory

Sanjay Sharma

Manav Rachna International Institute of Research and Studies

Biraj Kumar Sahoo

CSIR-National Metallurgical Laboratory

Krishna Guguloth

CSIR-National Metallurgical Laboratory

Research Article

Keywords: Creep life prediction, 316L stainless steel, Machine learning, High temperature deformation, Failure analysis

Posted Date: October 16th, 2026

DOI: https://doi.org/10.21203/rs.3.rs-11259809/v1

License: This work is licensed under a Creative Commons Attribution 4.0 International License.
Read Full License

Additional Declarations: No competing interests reported.

Machine Learning Assisted Creep Deformation Time Prediction and Failure Analysis of 316L Stainless Steel at Elevated Temperatures

Arun Kumar[1,2#], Sanjay Sharma[3], Biraj Kumar Sahoo[1], Krishna Guguloth[1*]

[1]Material Engineering Division, CSIR-National Metallurgical Laboratory, Jamshedpur-831007, India

[2]Center for Promotion of Research, Graphic Era Deemed to be University, Dehradun, India

[3]Research and Development Cell, Manav Rachna International Institute of Research and Studies, Faridabad, Haryana-121003, India

Corresponding author: #[arunkumarbit326@gmail.com]

*[krishna.nml@csir.res.in]

Abstract

Accurate prediction of creep deformation and rupture behavior is critical for evaluating the structural integrity and service life of metallic components operating at elevated temperatures. In this study, the high-temperature creep behavior and failure characteristics of 316L austenitic stainless steel were investigated experimentally at 675 °C and 725 °C under applied stresses of 175-245 MPa and 120-180 MPa, respectively. Three ensemble machine-learning models, Random Forest (RF), Extreme Gradient Boosting (XGBoost), and Light Gradient Boosting Machine (LightGBM) were developed using temperature, applied stress, and measured creep strain as input variables, with experimentally recorded deformation time as the prediction target. A 70:30 training-testing strategy and five-fold cross-validation were employed. For the combined temperature-stress dataset, XGBoost achieved the highest independent-testing coefficient of determination (($R^2 = 0.9945$)), whereas LightGBM yielded the highest five-fold cross-validation (R^2) of 0.9956. Conventional creep analysis yielded stress exponents of 6.9 at 675 °C and 4.5 at 725 °C, while the apparent creep activation energy was approximately (Qc = 324 kJ mol^{-1}). Larson–Miller analysis produced the strongest correlation at C = 22 (R^2 = 0.990). Post-creep SEM–EDS and fractographic analyses revealed Cr and Mo-rich carbide-containing regions associated with localized grain-boundary damage and a transition from predominantly dimpled microvoid coalescence at 675 °C/175 MPa to more pronounced cavity- and crack-associated damage at 725 °C/120 MPa. The results reveal an integrated framework

combining machine learning, creep kinetics, and post-creep damage characterization for interpreting creep degradation and failure of 316L stainless steel.

Keywords: Creep life prediction, 316L stainless steel, Machine learning, High temperature deformation, Failure analysis.

1. Introduction

316L austenitic stainless steel (ASS) is commonly used in high-temperature engineering applications, including power-generation [1, 2], nuclear [3, 4], automotive components [5], and chemical processing [6], and other systems in which corrosion resistance and mechanical stability are required [7-8]. However, prolonged exposure to elevated temperature under sustained mechanical loading can produce time-dependent creep deformation, microstructural degradation, damage accumulation, and eventual rupture [9, 10]. Reliable assessment of creep deformation and rupture life is essential for evaluating structural integrity, and remaining service life of components operating under severe thermo-mechanical conditions [11, 12]. In particular, an accurate description of the relationship between applied stress, temperature, creep deformation, and subsequent damage evolution is important for understanding the progression from time-dependent deformation to final failure.

Creep rupture life is commonly estimated using empirical and semi-empirical time-temperature parameters, including the Larson-Miller, Manson-Haferd approaches [13-15]. These methods provide convenient correlation among temperature, applied stress, and rupture time, but their predictive capability depends on the assumed functional form and the range of experimental data used for calibration. Such correlations are particularly useful for establishing global trends in rupture behavior, but they do not explicitly describe the nonlinear relationship between the evolving creep strain and the corresponding deformation time. In materials exhibiting nonlinear interactions among stress, temperature, deformation, and microstructural evolution, data-

driven methods can provide an alternative framework for representing experimentally observed relationships.

Machine-learning (ML) methods have increasingly been applied in materials engineering because they can represent nonlinear relationships among multiple variables without prescribing a specific constitutive form. Random Forest (RF), Extreme Gradient Boosting (XGBoost), and Light Gradient Boosting Machine (LightGBM) are particularly attractive for small- to medium-sized tabular datasets because of their ability to capture nonlinear feature interactions [16-18]. Recent studies have demonstrated the application of ML algorithms, including artificial neural networks (ANNs), support vector regression (SVR), and ensemble-learning methods, for predicting the creep and fatigue behavior and service life of metallic materials [19, 20]. More recently, ensemble algorithms, including RF, XGBoost, and LightGBM, have demonstrated strong predictive capabilities in materials science applications because of their ability to capture nonlinear relationships and interactions among multiple input variables [21, 22]. Hybrid and physics-informed ML approaches have also been increasingly investigated for creep-life prediction by incorporating experimental data, computational modelling, and physically meaningful descriptors [23,24]. Nevertheless, high statistical prediction accuracy alone does not establish the physical mechanisms responsible for creep deformation or rupture.

Our previous studies investigated the application of molecular-dynamics (MD) simulations combined with ML approaches to describe the deformation and creep behavior of Fe-Cr-Ni alloys [25, 26]. These studies demonstrated the potential of data-driven approaches for describing temperature and stress-dependent deformation behavior. However, computationally generated datasets and experimentally measured creep-rupture data represent different sources of materials information. Experimental creep testing directly incorporates the combined effects of material condition, temperature, applied stress, microstructural variability, and damage

evolution. Therefore, experimental validation of data-driven models using actual creep-rupture data is necessary to determine whether the relationships learned from computational or numerical datasets remain representative of experimentally observed material behavior. Several researchers have applied ML methods to creep-life prediction using experimental datasets for steels and other metallic materials [27-30]. Wang et al. [28] developed a Bayesian convolutional neural network with uncertainty quantification for creep-life prediction in steels, while Zare et al. [29] investigated ML-based prediction of creep lifetime in 9Cr-1Mo steel.

Despite these developments, an experimentally grounded framework that simultaneously examines ML-based creep-response prediction, conventional creep kinetics, and post-creep damage and fracture characteristics of 316L stainless steel under multiple temperature-stress conditions remain comparatively limited. More importantly, a high coefficient of determination obtained from ML models does not by itself demonstrate improved understanding of creep degradation, because the models primarily reproduce statistical relationships contained in the experimental dataset [31]. A more physically informative assessment therefore requires the ML results to be interpreted together with conventional creep parameters, including the stress exponent, apparent activation energy, and Larson–Miller parameter, as well as direct evidence of post-creep microstructural and fractographic damage. Such an integrated analysis can establish a clearer connection between the macroscopic creep response, data-driven prediction, and the underlying damage and failure characteristics.

Accordingly, the present study investigates the high-temperature creep and rupture behavior of 316L ASS at 675°C and 725°C under multiple applied stresses. Three ensemble ML models, RF, XGBoost, and LightGBM are evaluated for reproducing the experimentally recorded creep deformation-time response using temperature, applied stress, and measured creep strain as input variables. Conventional creep analysis is performed to quantify the stress dependence, temperature dependence, and rupture-life correlation through the stress exponent,

apparent activation energy, and Larson-Miller parameter. Post-creep SEM-EDS and fractographic analyses are further employed to identify localized grain-boundary (GB) damage, carbide-containing regions, cavity formation, crack development, and fracture characteristics. The study therefore aims to establish an integrated experimental–data-driven framework in which ML prediction is quantitatively evaluated and physically interpreted using conventional creep kinetics and post-creep damage observations. Particular attention is given to the distinction between reproducing experimentally recorded deformation-time behavior and making prospective predictions of previously unknown rupture life, thereby defining the applicability and limitations of the present ML framework.

2. Methodology

The overall workflow consisted of experimental creep testing, preparation of the experimentally measured creep dataset, machine-learning-based prediction of the recorded creep deformation-time response, conventional creep analysis, and post-creep microstructural and fractographic characterization. The workflow was designed to connect the measured macroscopic creep response with data-driven prediction and independent physical interpretation through conventional creep parameters and post-rupture observations. The overall framework is shown schematically in Fig.1.

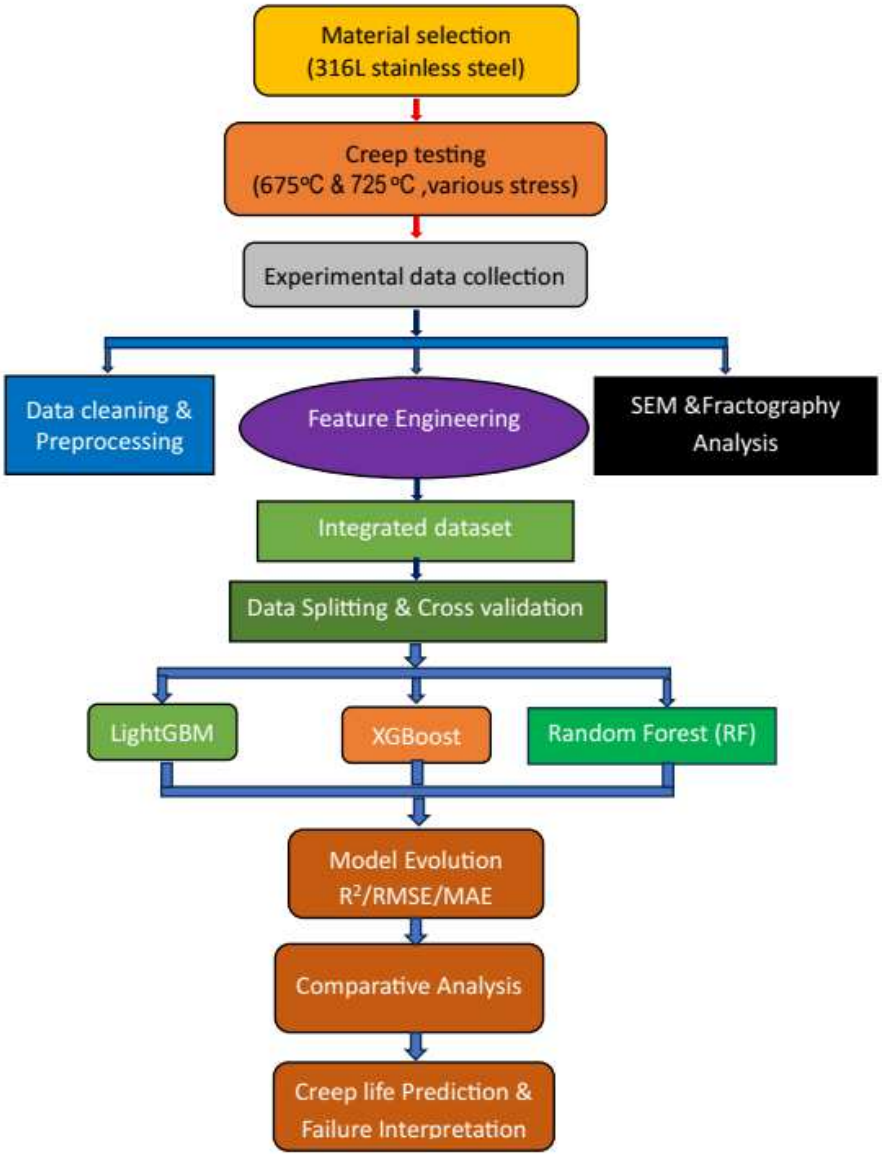


Figure 1 Schematic representation of the experimental and machine learning framework for prediction of experimentally recorded creep deformation time and failure analysis of 316L stainless steel.

2.1 Experimental creep testing

316L stainless steel was selected because of its corrosion resistance and mechanical stability at elevated temperatures. Standard creep specimens were prepared in accordance with ASTM E139 [32]. Constant load creep tests were conducted at 675 °C under applied stresses of 245, 210, and 175 MPa and at 725 °C under applied stresses of 180, 150, and 120 MPa. All creep

tests were continued until rupture, and the corresponding time-dependent creep strain was continuously recorded throughout each test. Temperature and applied load were controlled throughout each test to ensure consistency. The resulting creep curves were used both for conventional creep analysis and for constructing the machine-learning dataset.

After rupture, specimens were prepared for microstructure and fractographic examination by sequential polishing to 2500 grit, followed by alumina and colloidal-silica polishing. The polished surfaces were etched for 10 min using a modified (15 mL HCl + 5 mL HNO_3 + 5 mL glycerol) etchant, and examined using an SU7000 scanning electron microscope equipped for EDS analysis.

2.2 Data preparation and preprocessing

The experimental dataset comprised three input variables: test temperature (T), applied stress (σ), and experimentally measured creep strain (ε). The corresponding experimentally recorded deformation time was used as the output variable. Thus, the ML problem was formulated as a nonlinear mapping between temperature, applied stress, creep strain, and the corresponding recorded deformation time. Each data point represents a measured creep-strain value at a specific recorded time under a defined temperature and applied-stress condition. Therefore, the present ML formulation evaluates the ability of the models to reproduce the experimentally observed deformation-time response rather than directly predicting an unknown future rupture time from early-stage creep data.

Before model development, the dataset was preprocessed to remove inconsistencies and ensure data quality. The temperature, applied stress, and creep-strain values were retained as the model features, while the recorded deformation time was treated exclusively as the target variable. The dataset was divided into training and testing subsets using a 70:30 ratio.

Because the experimental measurements originate from individual creep curves, observations belonging to the same curve are physically correlated. This correlation was explicitly

considered when interpreting the validation results, and the present point-wise data split is therefore regarded as an assessment of predictive performance within the available experimental dataset rather than as complete specimen-level generalization [33, 34].

2.2 Machine learning models and evolution

Three ensemble learning algorithms Random Forest (RF), Extreme Gradient Boosting (XGBoost), and Light Gradient Boosting Machine (LightGBM) were employed to predict the experimentally recorded creep deformation time. These models were selected to provide complementary tree-based ensemble approaches for representing nonlinear interactions among temperature, applied stress, and creep strain.

RF is a bagging-based technique that reduces variance by averaging predictions from multiple decision trees constructed from randomly selected subsets of the data [35]. XGBoost and LightGBM are boosting-based methods that iteratively improve prediction performance by minimising a regularised loss function [36,37]. XGBoost incorporates L1 and L2 regularization to control model complexity, whereas LightGBM employs histogram-based learning and leaf-wise tree growth for computationally efficient gradient boosting. The models were trained separately for the 675°C dataset, the 725°C dataset, and the combined temperature–stress dataset. This enabled evaluation of model performance both within individual temperature regimes and across the complete experimental domain.

The hyperparameters of the three models were optimised through systematic parameter screening over predefined ranges. The selected hyperparameters are reported in Table 1. Predictive performance was assessed using mean absolute error (MAE), root mean square error (RMSE), and coefficient of determination (R^2) was calculated as follows:

Mean Absolute Error (MAE)

$$MAE = \frac{1}{n}\sum_{i=1}^{n}|y_i - \hat{y}_i| \quad (1)$$

Root Mean Square Error (RMSE)

$$RMSE = \sqrt{\frac{1}{n}\sum_{i=1}^{n}(y_i - \hat{y}_i)^2} \quad (2)$$

Coefficient of determination (R^2)

$$R^2 = 1 - \frac{\sum_{i=1}^{n}(Y_i - \hat{Y}_i)^2}{\sum_{i=1}^{n}(Y_i - \bar{Y})^2} \quad (3)$$

Where Y_i and $\hat{Y}_i$ represent the experimental and predicted values respectively, $\bar{Y}$ denotes the mean of actual values, and N is the total number of data points.

Table 1: Selected hyper parameter values for RF, LightGBM and XGBoost model for individual dataset.

	725 ºC				**675 ºC**				**Both Temperature**
Stress (MPa)	120	150	180	120, 150, 180	175	210	245	175, 210, 245	120, 150, 180, 175, 210, 245
RF									
n_estimator	100	100	100	100	100	100	100	100	100
min sample split	2	2	2	2	2	2	2	2	2
Max Depth	10	10	10	10	10	10	10	10	10
Min sample leaf	2	2	2	2	2	2	2	2	2
LightGBM									
n_estimator	150	150	150	150	150	150	150	150	150
Learning rate	0.03	0.03	0.04	0.03	0.8	0.8	0.03	0.09	0.2
Max Depth	10	10	10	10	10	10	10	10	10
Min child sample	12	12	12	12	10	10	8	8	12
Number of Leaves	4	4	4	4	4	4	4	4	4
XGBoost									
n_estimator	100	100	100	100	100	100	100	100	100
Learning rate	0.05	0.04	0.04	0.08	0.05	0.06	0.06	0.9	0.08
Max Depth	10	10	10	10	10	10	10	10	10
Min child weight	9	9	9	9	9	9	9	15	8

2.3 Model validation and hyperparameter optimisation

The machine-learning models were developed using a 70:30 training to testing split. The testing subset was kept completely independent from model training and hyperparameter optimization. Hyperparameters were optimized within predefined parameter ranges using five-fold cross-validation performed only on the training dataset. (R^2), RMSE, and MAE were used as the criteria for selecting the optimal hyperparameter combination.

After optimization, the final models were retrained using the complete training dataset with the selected hyperparameters and subsequently evaluated using the independent testing dataset. Thus, the reported testing performance was obtained only after completion of model training and hyperparameter optimization. An important consideration is that the present five-fold cross-validation was performed at the individual data-point level. Because multiple measurements originate from the same experimental creep curve, measurements from a given curve can occur in both training and validation folds. Consequently, the cross-validation results quantify model stability within the available dataset but should not be interpreted as fully independent specimen-level generalization. This distinction is important because the present study is intended to evaluate the ability of the ensemble models to reproduce experimentally measured creep deformation-time relationships within the investigated temperature, stress, and strain domain. Where independent creep-curve validation is performed in a subsequent analysis, the individual creep curve will be treated as the grouping unit so that all measurements from a given curve remain within either the training or testing subset. Such a curve-level analysis would provide a stricter assessment of generalization and should be reported separately from the present point-wise validation.

2.4 Conventional creep analysis

The effects of applied stress and temperature on creep behavior of 316L austenitic stainless steel were characterized by conventional creep parameters. The experimentally measured creep data were used to determine the stress exponent, Larson-Miller parameter (LMP) and apparent activation energy. The stress dependence of the minimum creep rate was evaluated using the Norton power-law relationship [38]:

$$\dot{\varepsilon}_{min} = A\sigma^{n} \tag{4}$$

where $\dot{\varepsilon}_{min}$is the minimum creep rate (h^{-1}), σ is the applied stress (MPa), A is a material-dependent constant, and n is the stress exponent. The stress exponent was obtained from the slope of a linear least squares regression of ln ($\dot{\varepsilon}_{min}$) against ln(σ)

Thus, the stress exponent n was determined from the slope of a linear least-squares regression of ln($\dot{\varepsilon}_{min}$) versus ln(σ). The analysis was performed separately for the three applied stress levels at 675 °C (175, 210, and 245 MPa) and 725 °C (120, 150, and 180 MPa). The resulting stress exponents were 6.9 and 4.5 at 675 °C and 725 °C, respectively.

The temperature dependence of creep rupture life was evaluated using the Larson-Miller parameter [39]:

$$LMP = T(C + log_{10}t_r) \tag{6}$$

where $T$is the absolute temperature (K), t_r is the experimentally measured rupture time (h), and C is the Larson-Miller material constant. LMP values were calculated using $C = 20$ and $C = 22$, and linear least-squares regression was performed between the calculated LMP and applied stress. The corresponding coefficients of determination were $R^2 = 0.970$ for $C = 20$ and $R^2 = 0.990$ for $C = 22$. Accordingly, $C = 22$ was used for the subsequent LMP analysis. The value providing the stronger correlation within the present experimental dataset was subsequently used for the LMP analysis.

The temperature dependence of the minimum creep rate was further evaluated using the Arrhenius-type relationship [40]:

$$\dot{\varepsilon}_{min} = A'\sigma^n \exp(-\frac{Q_C}{RT}) \tag{7}$$

where Q_c is the apparent creep activation energy (J mol^{-1}), R is the universal gas constant (8.314 J mol^{-1} K^{-1}), and $T$is the absolute temperature (K). The activation energy was obtained from the linear regression of the logarithm of minimum creep rate against inverse temperature (1/T). Experimentally obtained data at 625 °C were used only for the Arrhenius analysis to

extend the temperature range and were not included in the ML dataset or in the other comparative creep analyses.

2.5 Correlation of creep deformation time prediction with failure characteristics

The machine-learning predictions, conventional creep parameters and post-rupture microstructural observations were considered in conjunction to correlate the macroscopic creep response with the observed damage characteristics. SEM-EDS analysis was performed to investigate the local elemental distribution and morphology of regions related to creep damage. The observed Cr and Mo-enriched regions are consistent with carbide-containing precipitates commonly reported in 316L austenitic stainless steel during high temperature exposure and creep, particularly Cr-rich $M_{23}C_6$ type carbides at grain boundaries [41,42]. These grain boundary precipitates have been reported to influence localized creep damage and cavity formation in austenitic stainless steels [41,43]. Thus, the Cr- and Mo-enriched regions observed in the present study are discussed $M_{23}C_{6\ type}$ carbide containing regions, in agreement with the reported precipitation behavior of 316L stainless steel. The fractographic observations also indicated progressive cavity formation, growth and coalescence, with more pronounced cavity/crack coalescence at the higher testing temperature. These observations provide microstructural evidence for the creep damage and failure behavior observed in experiments.

3. Results and discussion

3.1 Experimental creep behavior

The experimentally measured creep behavior of 316L stainless steel at 675 °C and 725 °C under three applied stress levels at each temperature is shown in Fig. 2**.** The creep curves exhibit the characteristic progressive increase in creep strain with exposure time, followed by accelerated deformation approaching rupture. At 675 °C, the creep deformation time increased markedly as the applied stress decreased from 245 to 175 MPa. Similarly, at 725 °C, lowering

the applied stress from 180 to 120 MPa resulted in a substantial increase in the deformation time before rupture.

The comparison between the two temperatures also shows that creep deformation was considerably accelerated at 725 °C compared with 675 °C under the investigated conditions. This behavior is consistent with the increased contribution of thermally activated creep processes at higher temperature. The creep curves also show an extended low-strain deformation region followed by a pronounced increase in strain during the final stage of creep, indicating progressive acceleration toward rupture.

The experimental creep curves provide the direct basis for the subsequent machine-learning and conventional creep analyses. The measured strain-time data were used as the input response for the ML analysis, while the minimum creep rates and rupture times obtained from the same experiments were used to determine the conventional creep parameters. Thus, the experimental results establish the temperature- and stress-dependent creep response against which the data-driven predictions and creep life correlations are evaluated.

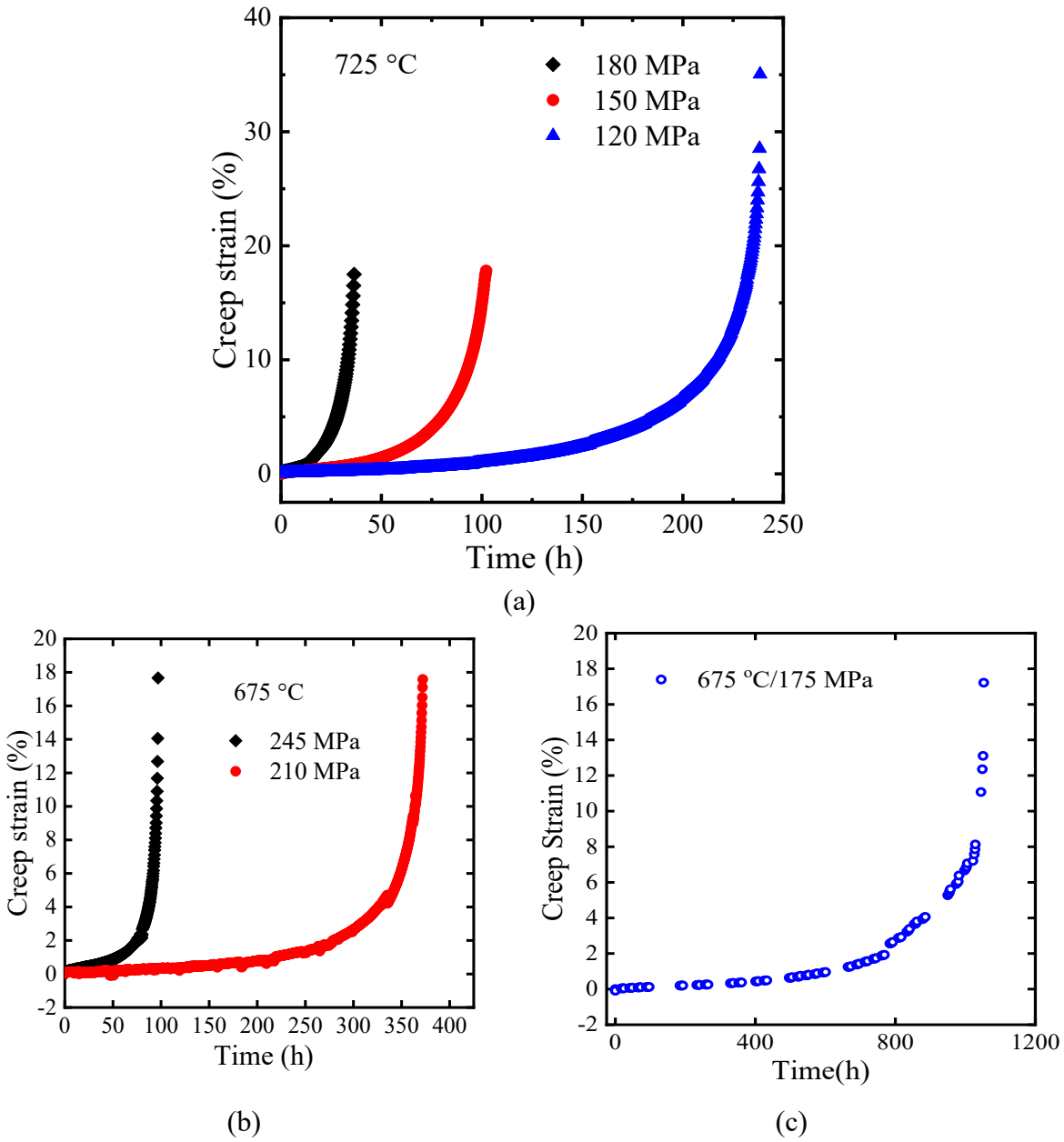


Figure 2 Experimentally measured creep strain–time curves of 316L stainless steel at (a) 725 °C under 180, 150 and 120 MPa, and (b, c) 675 °C under 245, 210 and 175 MPa.

3.2 Machine learning prediction at 675 ^{o}C

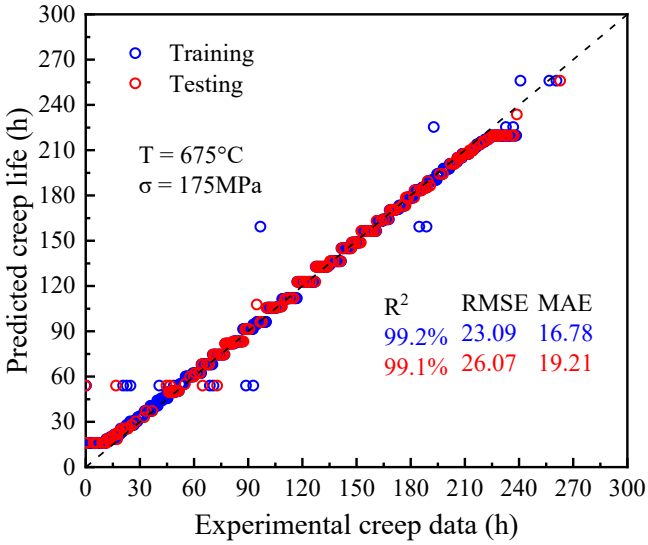
The creep curves at 675 °C show a clear stress-dependent change in deformation time, with the 175 MPa condition exhibiting the longest exposure and the 245 MPa condition the shortest. This variation is reflected directly in the machine-learning prediction performance. The models were therefore evaluated separately at 175, 210, and 245 MPa to examine how the creep-deformation regime influences prediction accuracy.

At 175 MPa, the results in Fig. 3 show close agreement between predicted and experimentally recorded deformation times for LightGBM, XGBoost, and RF. The testing R^2 values are 0.991, 0.993, and 0.994, respectively, while the corresponding RMSE values are 26.07, 22.60, and 21.77 h. The MAE values are 19.21, 15.67, and 16.94 h. Although the R^2 values remain high, the larger absolute errors indicate greater variability in the longer-duration creep response. At lower stresses, the deformation process is associated with prolonged exposure during which diffusion-assisted processes, vacancy transport, GB effects, and progressive damage evolution can contribute to local variations in the measured response [44-46]. Thus, the larger prediction uncertainty at 175 MPa is consistent with the greater time available for microstructural evolution rather than indicating a failure of the ML models to reproduce the overall trend.

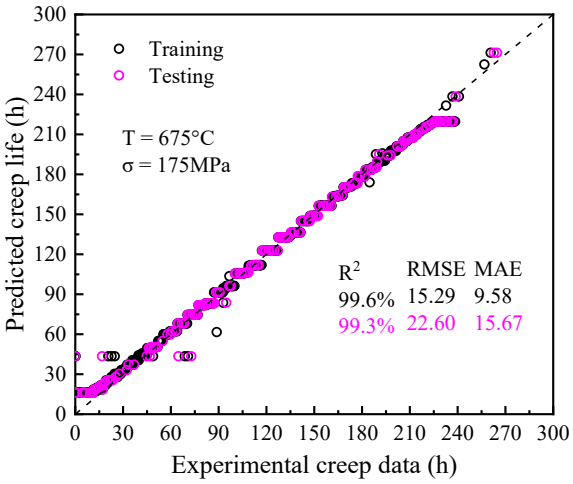
When the applied stress increases to 210 MPa, Fig. 4 shows a marked reduction in the prediction error. The testing RMSE values are 8.97 h for LightGBM, 9.28 h for XGBoost, and 11.57 h for RF, with corresponding MAE values of 6.28, 6.93, and 9.26 h. The testing R^2 values remain above 0.99 for all three models. The shorter deformation period and more strongly stress-driven response reduce the relative scatter in the experimental deformation-time relationship. The observed behavior is consistent with an increased contribution from stress-assisted dislocation-mediated deformation, although the stress exponent alone cannot uniquely define the controlling mechanism [46,47].

At the highest applied stress of 245 MPa, Fig. 5 shows further improvement in predictive agreement. The testing RMSE values decrease to 2.10, 1.87, and 2.38 h for LightGBM, XGBoost, and RF, respectively, while the corresponding MAE values are 1.50, 1.48, and 1.97 h. The testing R^2values remain approximately 0.995-0.996. The close clustering of the predicted values around the experimental data indicates that the deformation-time relationship becomes more consistent under this higher-stress condition. The relatively small errors may be associated with the shorter deformation period and stronger stress dependence of the creep response [47,48].

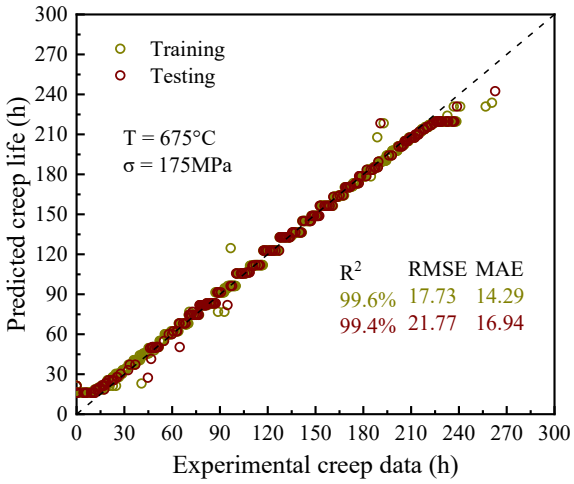
The stress-dependent results therefore reveal an important feature of the present dataset: prediction error decreases substantially as the applied stress increases. At 675 °C, the testing RMSE decreases from approximately 26 h at 175 MPa to approximately 2 h at 245 MPa, while the MAE decreases from approximately 19 h to 1.5 h. This does not mean that the higher-stress condition is intrinsically more representative of long-term creep behavior; rather, it indicates that the experimentally recorded deformation-time response is less dispersed within the investigated high-stress range. From a failure-analysis perspective, the larger uncertainty at lower stress is important because prolonged exposure provides more opportunity for microstructural degradation and damage accumulation.



(a) LightGBM

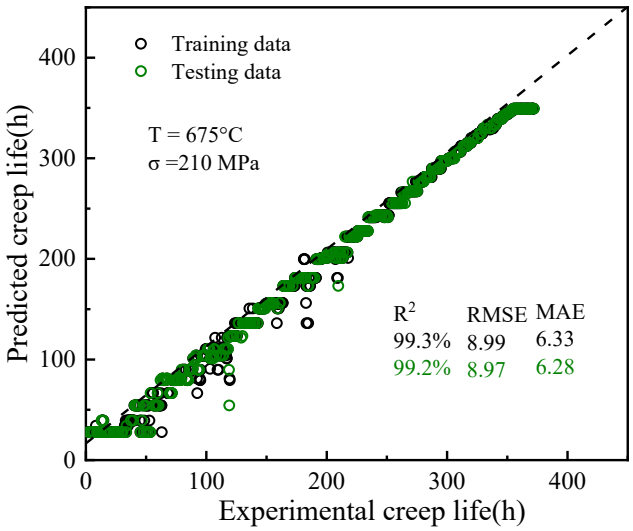


(b)XGBOOST

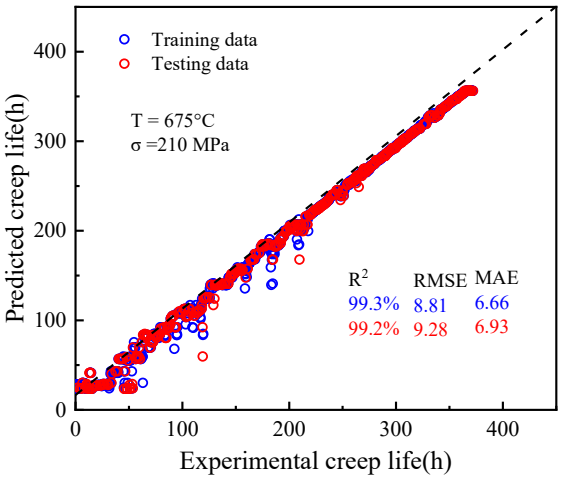


(c)Random Forest

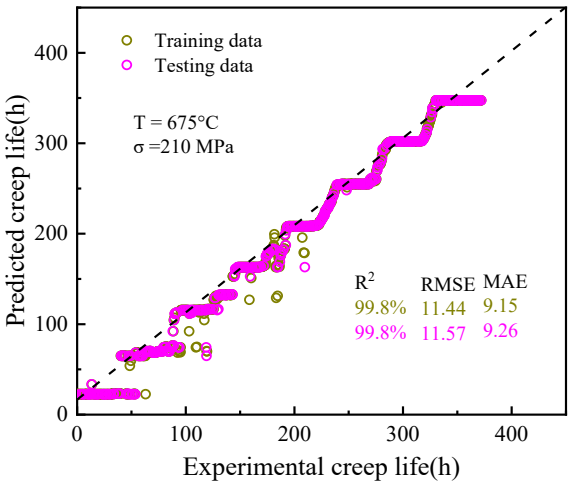
Figure 3 Comparison of predicted and experimental creep life of 316L stainless steel, tested at 675°C under an applied stress of 175 MPa results, using different machine learning models.



(a) LightGBM

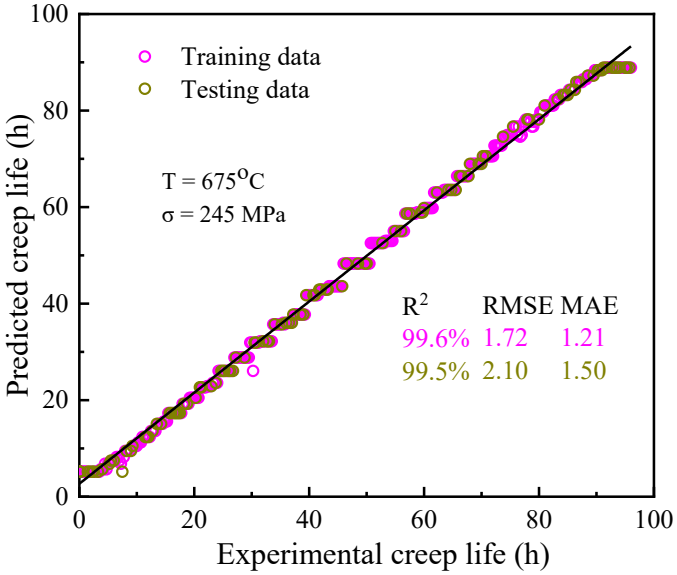


(b) XGBOOST

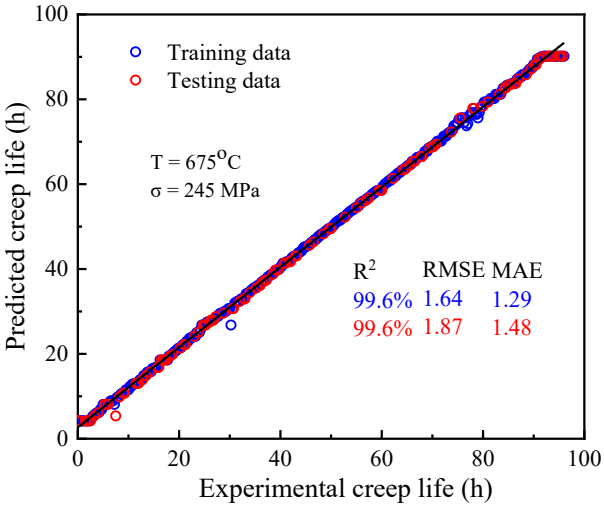


(c) Random Forest

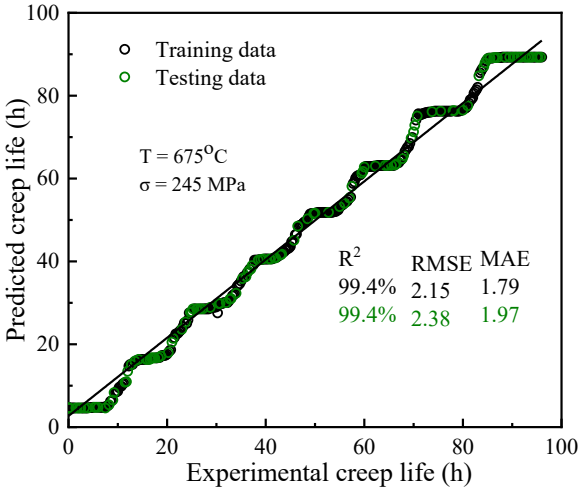
Figure 4 Comparison of predicted and experimental creep life of 316L stainless steel, tested at 675ºC under an applied stress of 210 MPa results using different machine learning models.



(a) LightGBM



(a) XGBOOST



(b) Random Forest

Figure 5 Comparison of predicted and experimental creep life of 316L stainless steel, tested at 675°C under an applied stress of 245 MPa results, using different machine learning models.

3.3 Machine learning prediction at 725°C

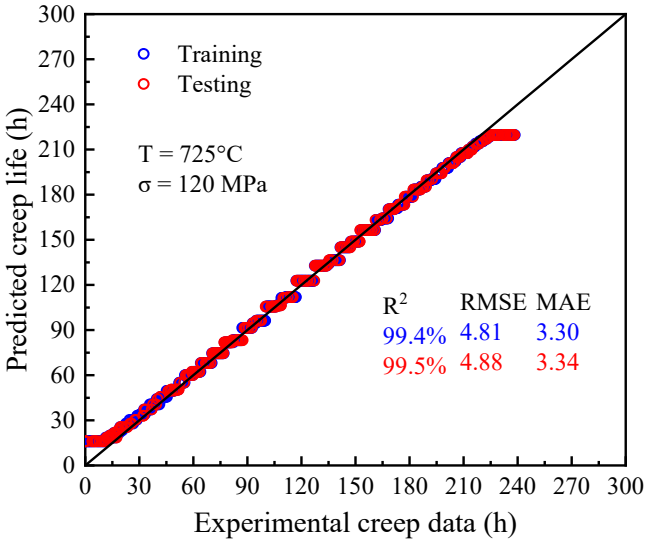
At 725 °C, the experimental curves in Fig. 2 show the same general progression from transient deformation to accelerated deformation, but over a shorter overall time scale than at 675 °C. Reducing the applied stress from 180 to 120 MPa progressively extends the deformation period. This combined temperature-stress dependence provides a basis for evaluating whether the ML models can reproduce the measured response under a more rapidly evolving creep condition.

At 120 MPa, Fig. 6 shows good agreement between the predicted and experimentally recorded deformation times. The testing R^2 values for LightGBM, XGBoost, and RF are 0.995, 0.996, and 0.992, respectively. The corresponding RMSE values are 4.88, 4.23, and 6.23 h, while the MAE values are 3.34, 2.99, and 5.34 h. The larger absolute errors relative to the higher-stress conditions are consistent with the longer deformation duration and the greater opportunity for microstructural degradation during creep exposure. Diffusion-assisted processes and GB effects can contribute to deformation variability under prolonged creep conditions [44-46].

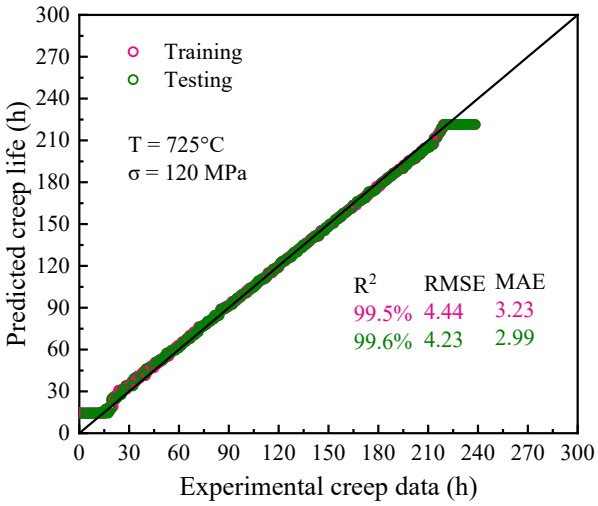
Increasing the stress to 150 MPa produces a reduction in prediction error, as shown in Fig. 7. The testing RMSE values are 3.06, 3.32, and 2.68 h for LightGBM, XGBoost, and RF, respectively. The corresponding MAE values are 2.20, 2.33, and 2.14 h. The relatively similar errors obtained from the three models indicate that the experimentally recorded deformation-time relationship remains consistently represented at this intermediate stress level. At 180 MPa, Fig. 8 shows the closest correspondence between predicted and experimental deformation times. The testing RMSE values are 0.71 h for LightGBM, 0.83 h for XGBoost, and 0.54 h for RF, with MAE values of 0.50, 0.59, and 0.41 h, respectively. The testing R^2 values are 0.996, 0.994, and 0.998. The lowest error at this condition occurs for RF, demonstrating that model performance is condition-dependent and that no single algorithm provides the lowest error at every stress level.

A similar stress-dependent reduction in prediction error is therefore observed at 725 °C. The testing RMSE decreases from approximately 6 h at 120 MPa to less than 1 h at 180 MPa, while the MAE decreases from approximately 5.5 h to approximately 0.5 h. The higher temperature accelerates the creep response, while increasing stress further shortens the deformation period and produces a more compact deformation-time relationship. The ML models capture this experimentally observed relationship, but they should not be interpreted as mechanistic models. The physical interpretation of the temperature- and stress-dependent response requires the complementary creep-kinetic and microstructural analyses presented below.

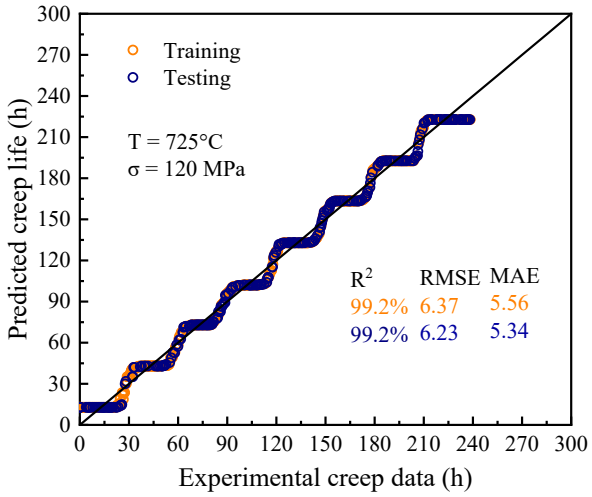
Table 2 presents statistical performance, which aligns with Figures 3-5 and Figure 6-8. All models exhibit high accuracy ($R^2 > 0.99$) under all stress and temperature conditions. A clear stress-related decrease in prediction error is seen. At 675 °C, RMSE lowers from 26 h (175 MPa) to 2 h (245 MPa), while MAE decreases from 19 h to 1.5 h. Similarly, at 725 °C, RMSE reduces from 6 h (120 MPa) to <1 h (180 MPa), and MAE from 5.5 h to 0.5 h. At lower stress, XGBoost and LightGBM show superior performance, whereas RF becomes competitive at greater stress and has the lowest RMSE (0.54 h at 180 MPa). The decrease in prediction error with increasing stress reflects the reduced dispersion of the experimentally recorded deformation-time response within the investigated stress range and does not, by itself, establish a transition between creep mechanisms. These findings demonstrate that the models properly account for the combined effect of stress and temperature on creep life prediction. Thus, the experimental stress dependency is consistently reflected in the ML prediction findings, implying that the models account for the combined effects of applied stress and temperature on creep rupture life.



(a) LightGBM

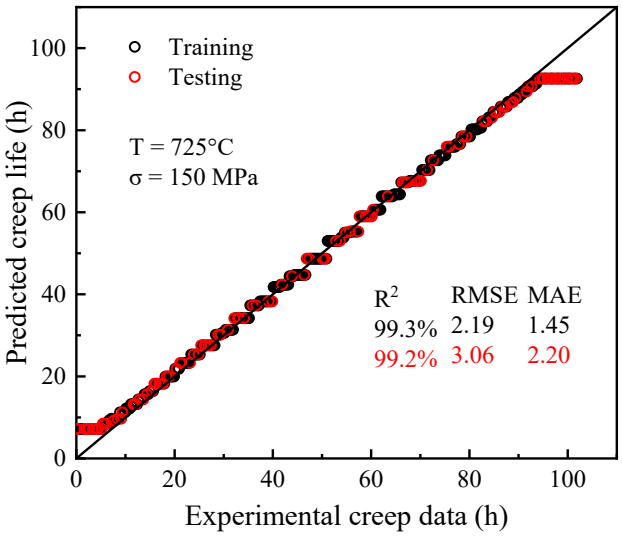


(b) XGBOOST

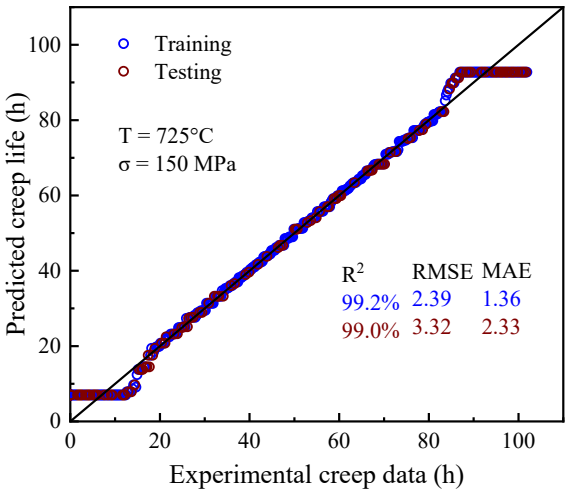


(c) Random Forest

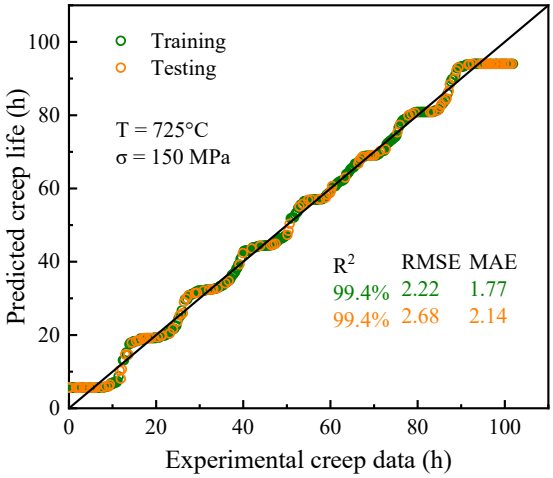
Figure 6 Comparison of predicted and experimental creep life of 316L stainless steel, tested at 725 ºC under an applied stress of 120 MPa results, using different machine learning models.



(a) LightGBM

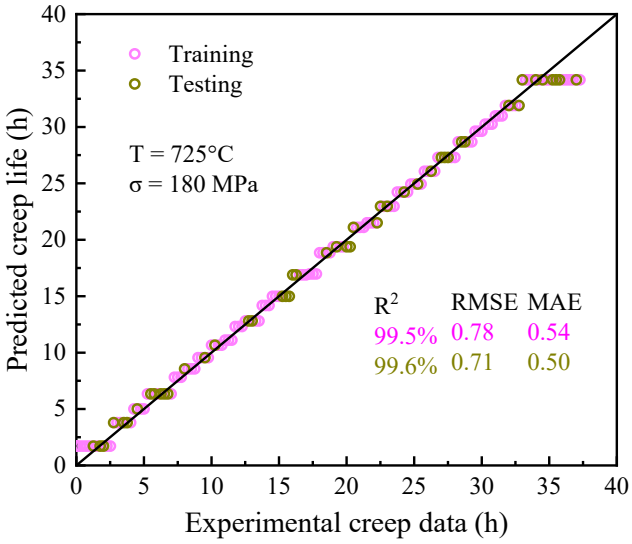


(b) XGBOOST

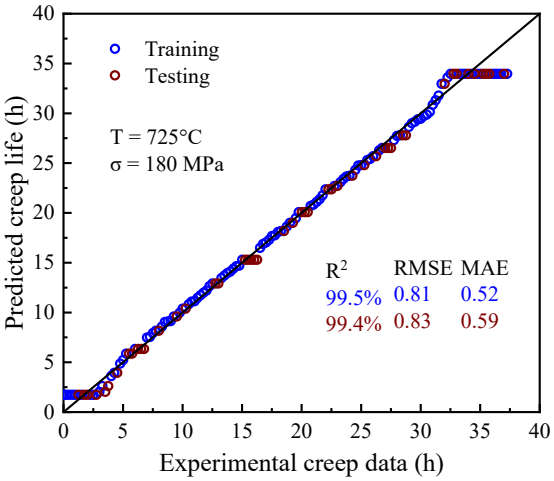


(c) Random Forest

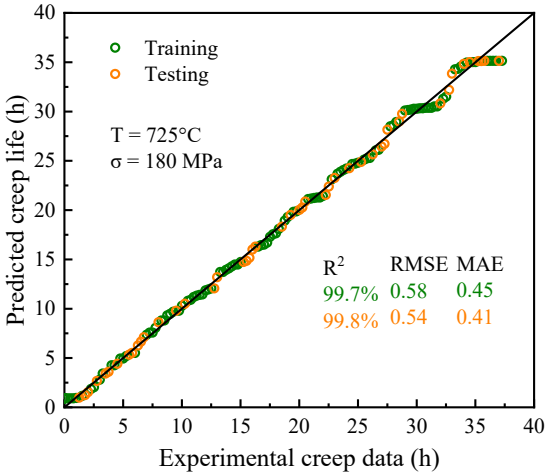
Figure 7 Comparison of predicted and experimental creep life of 316L stainless steel, tested at 725 °C under an applied stress of 150 MPa, results using different machine learning models.



(a) LightGBM



(b) XGBOOST



(c) Random Forest

Figure 8 Comparison of predicted and experimental creep life of 316L stainless steel, tested at 725 °C under an applied stress of 180 MPa, results using different machine learning models.

Table 2: Statistical evolution of predictive model performance across various applied stresses and temperatures.

Temperature (°C)	Applied stress (MPa)	Machine learning predictive model									
		LightGBM			XGBoost			RF			
		Metric	Training	Testing	Metric	Training	Testing	Metric	Training	Testing	
		R^2	0.995247	0.994921	R^2	0.995941	0.996026	R^2	0.991658	0.991735	
	120	RMSE	4.810891	4.885365	RMSE	4.445567	4.321242	RMSE	6.37311	6.231851	
		MAE	3.307283	3.347353	MAE	3.238351	2.997882	MAE	5.568331	5.345384	
		R2	0.993981	0.991798	R2	0.992818	0.990339	R2	0.993787	0.99368	
725	150	RMSE	2.191571	3.060631	RMSE	2.393888	3.321735	RMSE	2.226594	2.686677	
		MAE	1.457033	2.202056	MAE	1.363742	2.336374	MAE	1.77044	2.146419	
		R2	0.994947	0.995837	R2	0.994551	0.994407	R2	0.99724	0.997583	
	180	RMSE	0.787122	0.716494	RMSE	0.817363	0.83049	RMSE	0.581674	0.545987	
		MAE	0.544446	0.503585	MAE	0.521388	0.596103	MAE	0.450419	0.416946	
		R2	0.992636	0.991218	R2	0.996773	0.993398	R2	0.995658	0.993879	
	175	RMSE	23.09684	26.07585	RMSE	15.29043	22.60971	RMSE	17.73556	21.77003	
		MAE	16.78052	19.21443	MAE	9.583012	15.67422	MAE	14.29109	16.94631	
		R2	0.993072	0.992996	R2	0.993348	0.992519	R2	0.9888	0.98837	
675	210	RMSE	8.99764	8.979459	RMSE	8.816346	9.28014	RMSE	11.44045	11.57069	
		MAE	6.339536	6.281218	MAE	6.666635	6.938915	MAE	9.154301	9.261422	
		R2	0.996026	0.995175	R2	0.996399	0.996155	R2	0.993829	0.99382	
	245	RMSE	1.729948	2.105783	RMSE	1.646847	1.879772	RMSE	2.155861	2.38303	
		MAE	1.217825	1.50055	MAE	1.293312	1.489924	MAE	1.792437	1.976537	

3.4 Comparative analysis of machine learning models

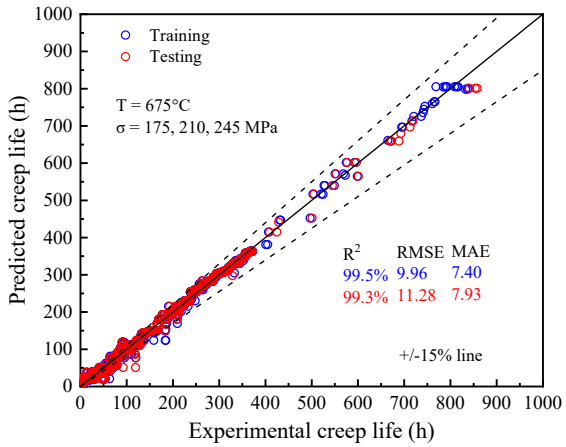
The stress-specific results are complemented by an overall comparison of the three models at each temperature. The results in Fig. 9 compare LightGBM, XGBoost, and RF for the three stress levels at 675 °C, while Fig. 10 presents the corresponding comparison at 725 °C.

At 675 °C, most predicted values lie within the ±15% deviation region in Fig. 9. The testing RMSE values are 11.28 h for LightGBM, 10.60 h for XGBoost, and 13.70 h for RF, with MAE values of 7.93, 5.89, and 7.16 h, respectively. At 725 °C, Fig. 10 shows similarly close agreement, with testing RMSE values of 4.47, 4.86, and 4.87 h for LightGBM, XGBoost, and RF, respectively. The corresponding MAE values are 3.68, 3.71, and 4.16 h.

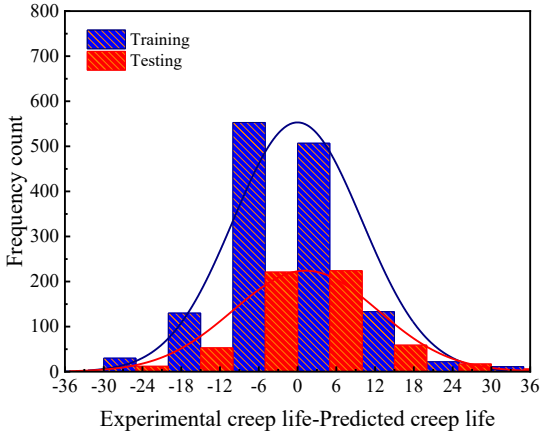
The residual distributions in Figs. 9 and 10 are generally centred around zero, indicating the absence of a pronounced systematic offset between predicted and experimental deformation

times. XGBoost and LightGBM exhibit relatively compact residual distributions, whereas RF shows a somewhat broader spread in the combined comparisons. However, the stress-specific results demonstrate that RF can perform competitively, particularly at the higher-stress conditions. Therefore, the model behavior is better interpreted in terms of condition-specific performance rather than as a universal ranking of the three algorithms.

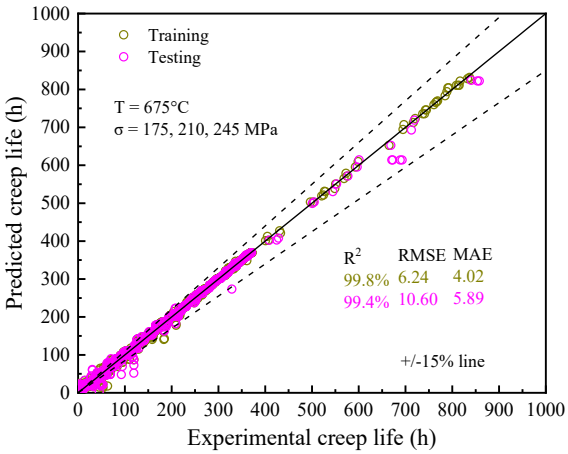
The statistical results in Table 2 confirm this trend. At both temperatures, the prediction error decreases with increasing applied stress. This behavior is consistent with the experimentally observed reduction in deformation duration and does not by itself establish a change from one unique creep mechanism to another. Rather, it indicates that the measured deformation-time relationship becomes less dispersed as stress increases within the investigated experimental domain.



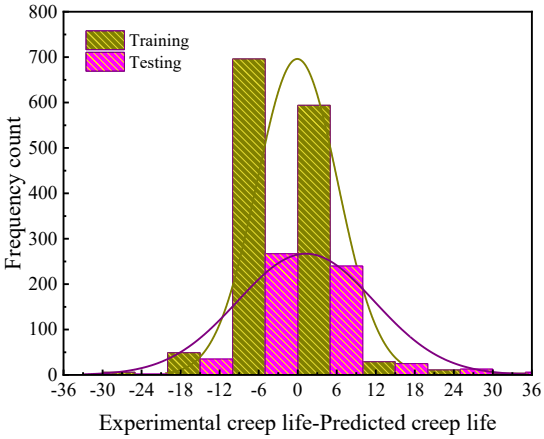
(a)



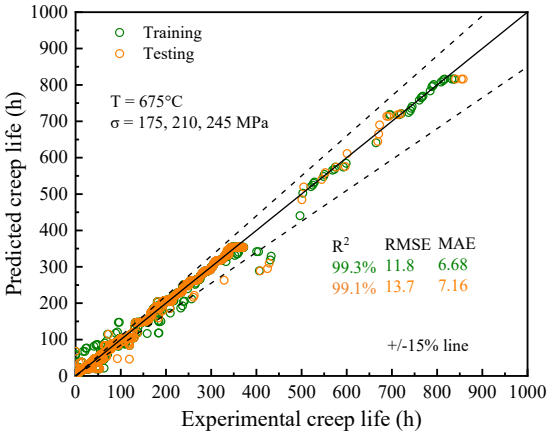
(b)



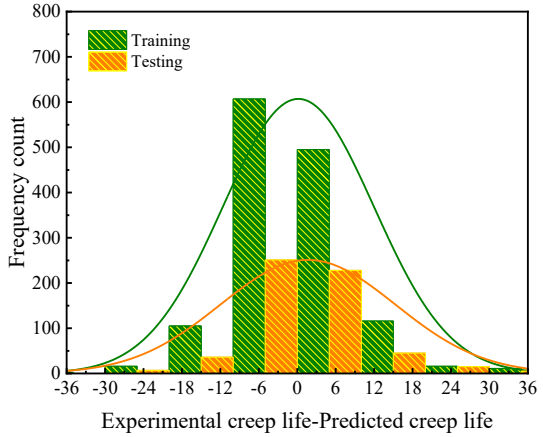
(c)



(d)



(e)



(f)

Figure 9 Comparative evaluation of (a-b) LightGBM, (c-d) XGBoost, and (e-f) Random Forest models for creep life prediction of 316L stainless steel, tested at 675 °C under varying applied stresses: correlation with experimental data and corresponding residual distribution.

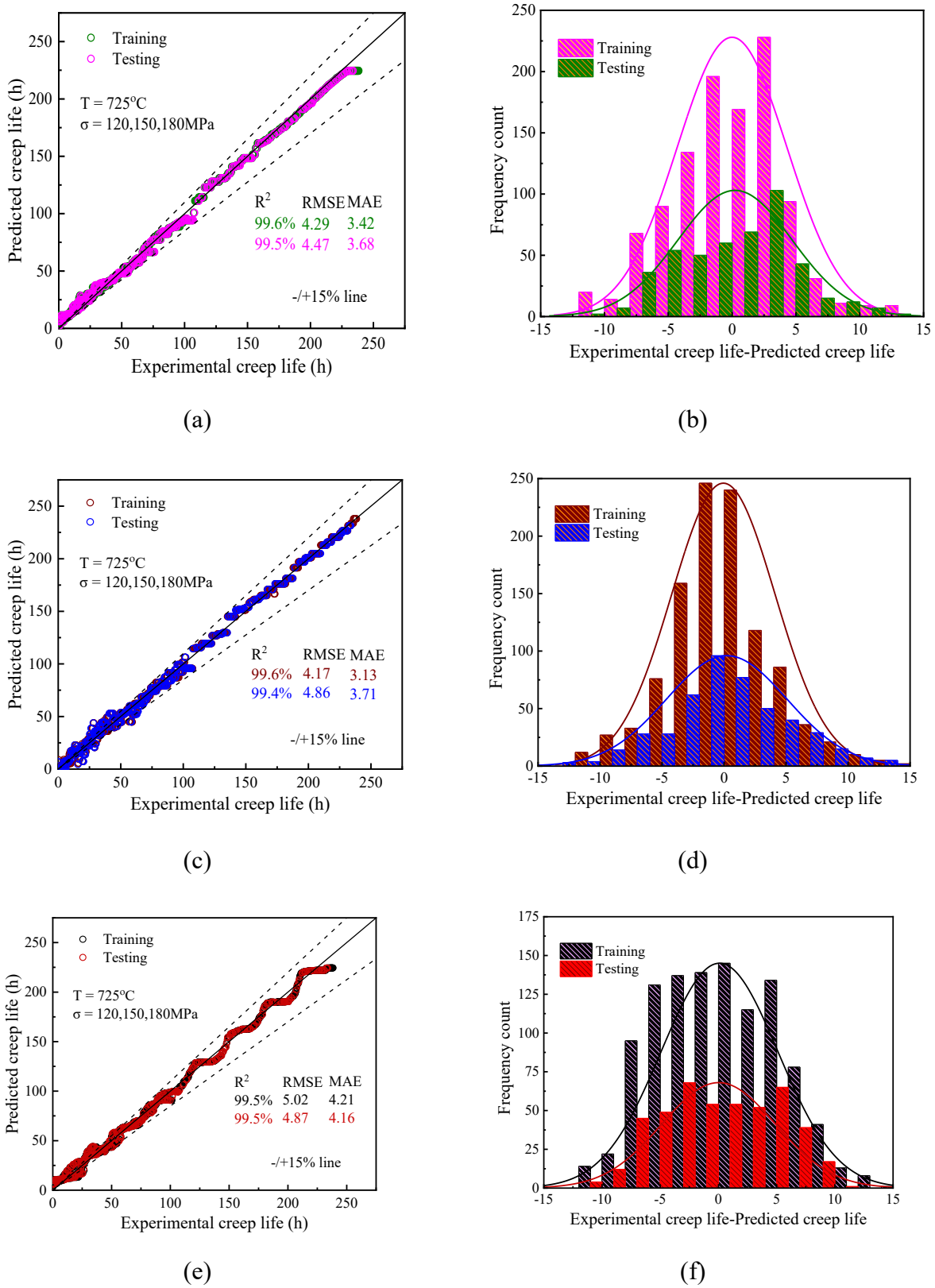


Figure 10 Comparative evaluation of (a-b) LightGBM, (c-d) XGBoost, and (e-f) Random Forest models for creep life prediction of 316L stainless steel, tested at 725 °C under varying applied stresses: correlation with experimental data and corresponding residual distribution.

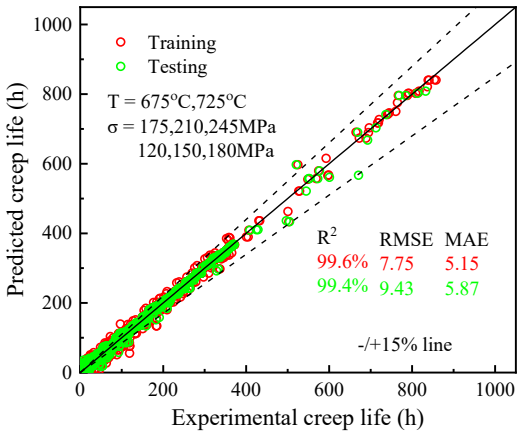
3.5 Combined dataset analysis across temperatures

To evaluate the response under simultaneous variation of temperature and applied stress, the complete dataset from 675 and 725 °C was analysed together. The resulting prediction and residual distributions are presented in Fig. 11, and the corresponding statistical results are listed in Table 3**.**

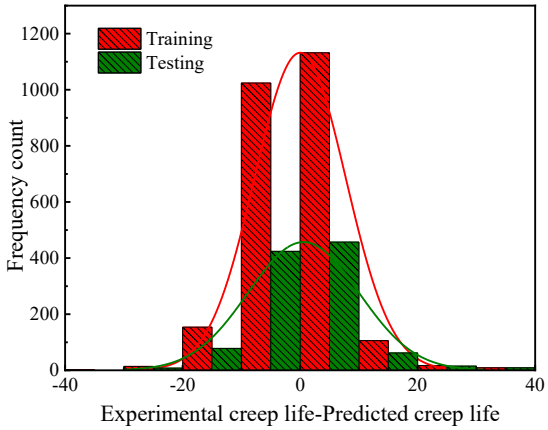
Despite the increased range of temperature and stress conditions, all three models reproduce the experimentally recorded deformation times with high R^2 values. XGBoost gives a training $R^2$of 0.998 and a testing R^2 of 0.9945, with testing RMSE and MAE values of 9.06 and 4.60 h, respectively. LightGBM gives testing $R^2 = 0.9940$, RMSE = 9.43 h, and MAE = 5.87 h, whereas RF gives testing $R^2 = 0.9851$, RMSE = 14.90 h, and MAE = 8.11 h.

The residual distributions in Fig. 11 are centred predominantly around zero, while most predicted values remain within the ±15% deviation region. This indicates that the models reproduce the nonlinear relationships contained in the experimental dataset over the investigated temperature–stress domain. The somewhat wider residual spread for RF indicates greater variability in its predicted deformation times for the combined dataset, whereas the boosting models provide a more compact representation of the experimental response.

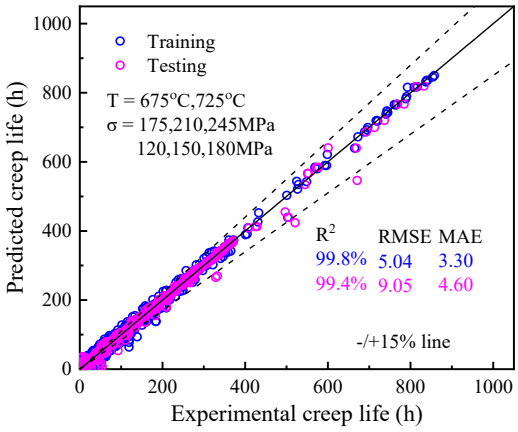
The higher performance of the boosting models is consistent with their ability to represent nonlinear interactions among multiple input variables [16-18]. However, the close agreement between training and testing results should be interpreted cautiously because individual points from the same creep curve are not statistically independent. Consequently, the present results demonstrate strong performance for held-out data points within the available dataset but should not be interpreted as fully independent specimen-level generalization. Validation using independent creep curves or additional specimens would provide stronger evidence of transferability.



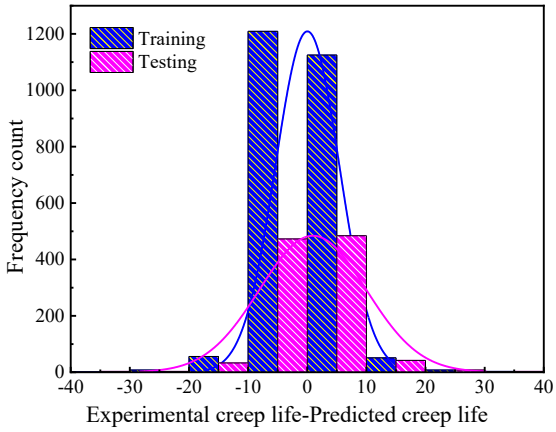
(a)



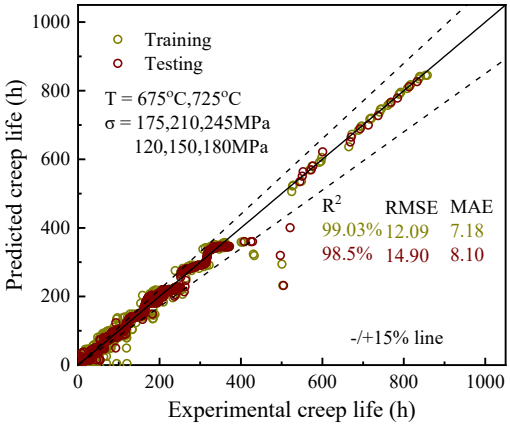
(b)



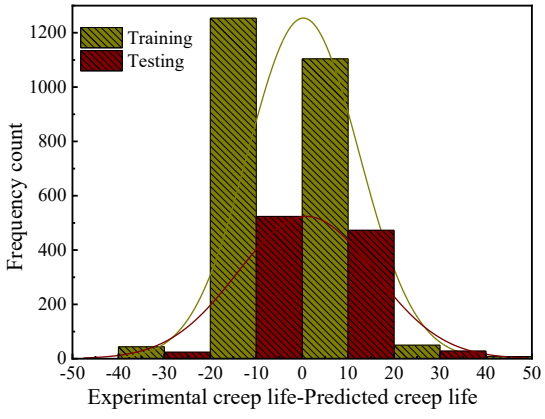
(c)



(d)



(e)



(f)

Figure 11 Comparative performance of (a-b) LightGBM, (c-d) XGBoost, and (e-f) Random Forest models for creep life prediction of 316L stainless steel, tested at 675 °C and 725 °C under varying applied stresses, showing agreement with experimental data and corresponding residual distributions.

Table 3: Performance evaluation of machine learning models for creep life prediction of 316L ASS.

Condition Parameter	Machine learning predictive model									
675°C Stresses: 175, 210, 245 MPa	LightGBM				XGBoost				RF	
	Metric	**Training**	**Testing**		**Metric**	**Training**	**Testing**		**Metric**	**Training**	**Testing**
	R^2	0.995247	0.994921		R^2	0.995941	0.996026		R^2	0.991658	0.991735
	RMSE	4.810891	4.885365		RMSE	4.445567	4.321242		RMSE	6.37311	6.231851
	MAE	3.307283	3.347353		MAE	3.238351	2.997882		MAE	5.568331	5.345384
725°C Stresses: 120, 150, 180 MPa	R^2	0.993981	0.991798		R^2	0.992818	0.990339		R^2	0.993787	0.99368
	RMSE	2.191571	3.060631		RMSE	2.393888	3.321735		RMSE	2.226594	2.686677
	MAE	1.457033	2.202056		MAE	1.363742	2.336374		MAE	1.77044	2.146419
675°C & 725°C Stresses: 175, 210, 245 MPa 120, 150, 180 MPa	R^2	0.996027	0.994035		R^2	0.99807	0.994497		R^2	0.990332	0.985101
	RMSE	7.754007	9.430186		RMSE	5.40473	9.057484		RMSE	12.09616	14.90393
	MAE	5.151931	5.873392		MAE	3.304474	4.601147		MAE	7.185907	8.109593

3.6 Cross-validation and model generalization

Five-fold cross-validation was performed on the training data to examine the stability of the developed models under different training–validation partitions. The R^2 values are summarized in Table 4.

For the combined stresses at 725 °C, the cross-validation R^2 values are 0.9944, 0.9952, and 0.9960 for RF, LightGBM, and XGBoost, respectively. At 675 °C, the corresponding values are 0.9912, 0.9946, and 0.9947. When both temperatures and all stress levels are combined, the cross-validation R^2 values are 0.9868 for RF, 0.9956 for LightGBM, and 0.9941 for XGBoost. The cross-validation results are broadly consistent with the independent testing results and indicate stable performance within the available data structure. However, the folds were generated at the individual data-point level. Since multiple measurements originate from the same creep curve, observations within a curve can be correlated. Therefore, the cross-validation results should be considered an assessment of model stability within the present dataset rather than definitive specimen-level generalization. This distinction is particularly

important for engineering failure assessment, where performance on independent creep curves is more representative of practical deployment.

Table 4: Five-fold cross validation results (R^2) for the developed machine learning models under different temperature and stress conditions.

	725 ºC				675 ºC				Both Temperature
Applied stress (MPa)	120	150	180	120, 150, 180	175	210	245	175, 210, 245	120, 150, 180, 175, 210, 245
RF	0.991456	0.993724	0.997468	0.994407	0.993241	0.988426	0.993783	0.991235	0.986786
LightGBM	0.995134	0.99248	0.99513	0.995206	0.990867	0.993053	0.99482	0.994612	0.995621
XGBoost	0.996087	0.990635	0.994501	0.996029	0.993972	0.993294	0.996117	0.994737	0.994054

3.7 Temperature-stress relationship and creep behavior

The experimental results and ML predictions are further interpreted using conventional creep parameters. Increasing either the testing temperature or applied stress accelerates the creep response, resulting in shorter deformation times and reduced rupture life. The experimentally observed stress–rupture-time relationship at 675 °C and 725 °C is presented in Fig. 12.

The Norton relationship gives stress exponents of 6.9 at 675 °C and 4.5 at 725 °C**.** The decrease in $n$with increasing temperature indicates that the stress dependence of the minimum creep rate changes between the two testing temperatures. Such a change may reflect a variation in the relative contributions of dislocation-mediated and diffusion-assisted deformation processes [28,47-49]. However, the stress exponent alone cannot uniquely identify the rate-controlling mechanism. Its interpretation therefore requires consideration of the activation energy and post-creep microstructural observations. The machine-learning results are consistent with this thermomechanical dependence because the models reproduce the changes in deformation time associated with temperature and stress. The ML analysis therefore provides a statistical description of the observed response, whereas the Norton analysis provides a conventional kinetic measure of stress sensitivity.

The Larson-Miller analysis in Fig. 13 further evaluates the combined effect of temperature and rupture time. For $C = 20$, the coefficient of determination is $R^2 = 0.970$, whereas increasing the constant to $C = 22$ gives $R^2 = 0.990$. Thus, $C = 22$ provides the stronger correlation for the present experimental dataset. Nevertheless, this result should be viewed as an empirical time–temperature correlation and not as a direct representation of microstructural evolution or a unique failure mechanism [13-15].

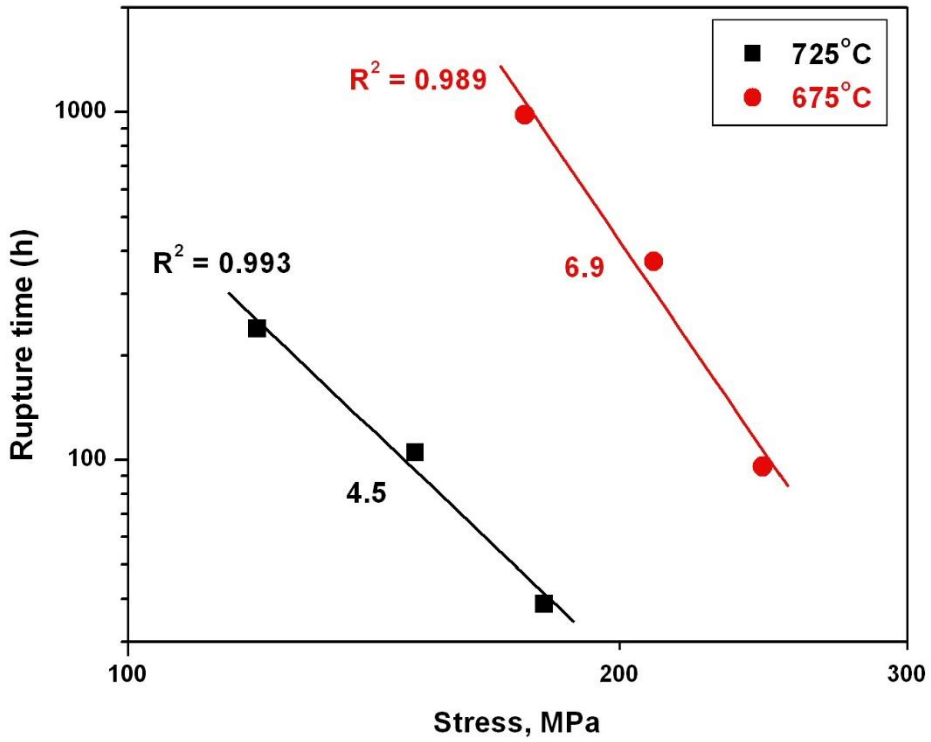
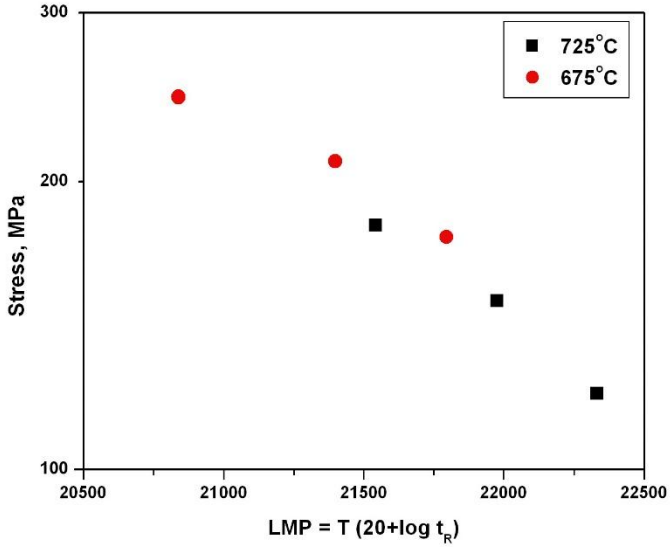


Figure 12 Stress-rupture time relationship used to determine the creep stress exponent at 675 °C and 725 °C.

(a)



(b)

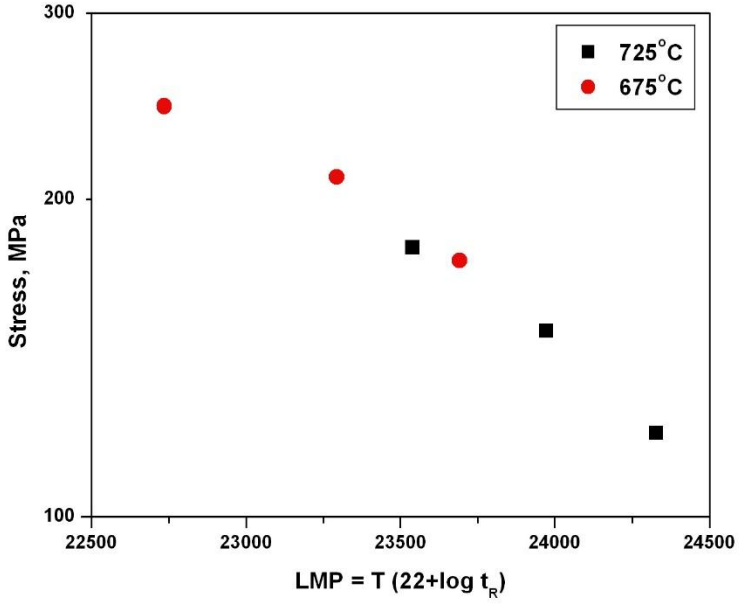
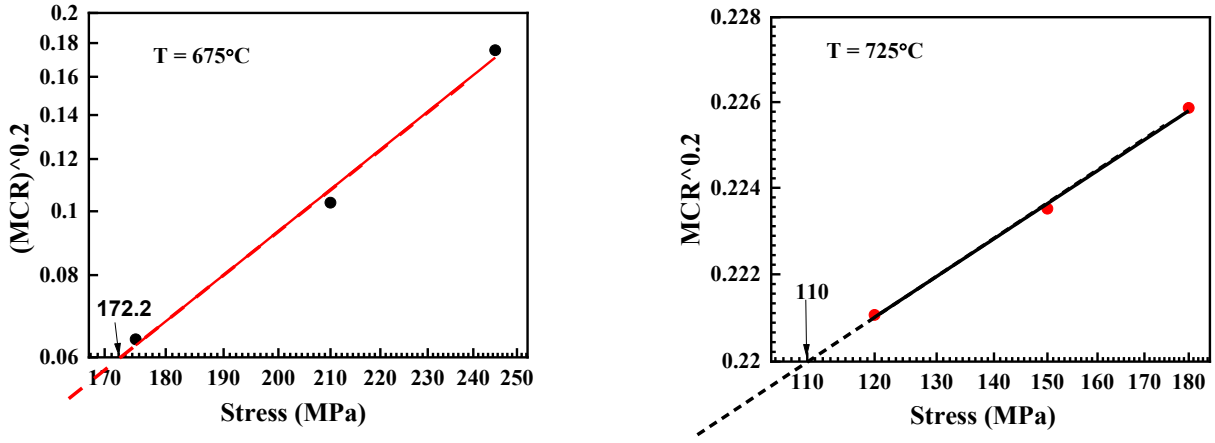


Figure 13 Larson-Miller parameter as a function of applied stress for 316L stainless steel used and evaluated at different material constants: (a) C = 20 and (b) C = 22.

3.8 Threshold stress and apparent activation energy

The threshold-stress analysis in Fig. 14 shows an apparent threshold stress of approximately 172.2 MPa at 675 °C and approximately 110 MPa at 725 °C. The lower apparent threshold stress at the higher temperature indicates a reduced resistance to thermally activated deformation. This behavior is consistent with enhanced atomic diffusion and facilitated dislocation motion at elevated temperature [50,51].

The Arrhenius analysis in Fig. 15 gives an apparent creep activation energy of approximately 324 kJ mol^{-1}**.** The 625 °C data were included only to extend the temperature range for this regression and were not used in the machine-learning dataset or other comparative analyses. The magnitude of the obtained activation energy is consistent with thermally activated processes involving atomic diffusion and dislocation motion reported for austenitic stainless steels [44,45,52]. However, the activation energy should not be interpreted as proof of a single rate-controlling mechanism. The observed creep behavior results from the combined effects of temperature, stress, deformation kinetics, and microstructural evolution. Accordingly, the stress exponent, threshold stress, activation energy, and post-creep damage observations should be considered together when interpreting the deformation behavior.



(a) (b)

Figure 14 Determination of threshold stress in 316L austenitic stainless steel through linear extrapolation method at two different temperatures: (a) 675 °C and (b) 725 °C.

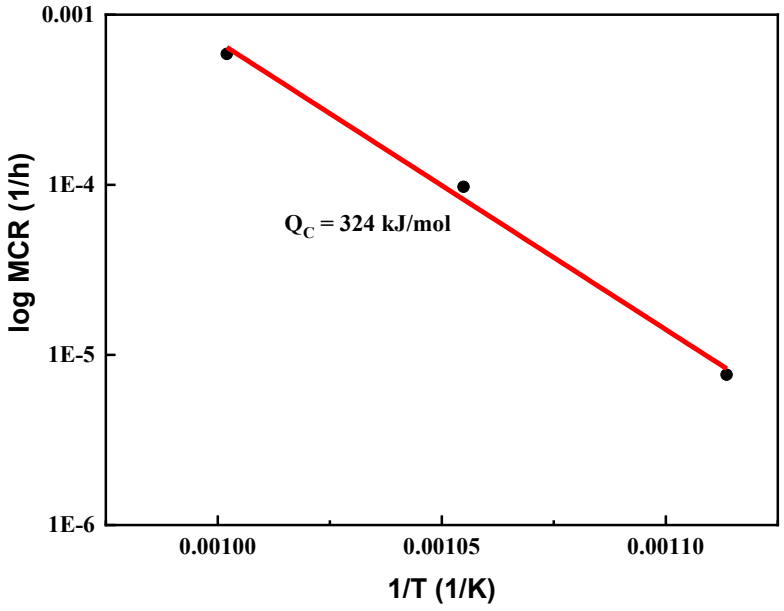


Figure 15 Arrhenius plot of minimum creep rate versus inverse of testing temperature (1/T) used to determine the apparent creep activation energy of 316L ASS, using creep data obtained at 625, 675, and 725 °C.

3.9 Fractography and post-creep microstructural analysis

The fracture and post-creep microstructural observations provide the direct failure-analysis component of the present study. Representative fracture surfaces at 675 °C/175 MPa and 725 °C/120 MPa are shown in Fig. 16.

At 675 °C/175 MPa, Fig. 16(a-c) shows a predominantly dimpled fracture morphology with microvoids and well-developed dimples. This morphology is consistent with ductile fracture through microvoid nucleation, growth, and coalescence. The developed dimples indicate that substantial localized plastic deformation occurred before final rupture. By comparison, the fracture surface at 725 °C/120 MPa in Fig. 16(d-f) is more irregular and contains elongated crack-like features and localized surface separation. These features are consistent with greater involvement of GB damage and creep cavitation in the final fracture process. However, the two representative conditions differ in both temperature and applied stress. Therefore, the observed difference in fracture morphology should be interpreted as the combined effect of these two variables rather than as an isolated temperature effect.

The post-creep microstructure at 675 °C/175 MPa is presented in Fig. 17. The low-magnification image shows the austenitic grain structure and annealing twin boundaries, together with localized damage near susceptible GB regions. The higher-magnification images reveal intergranular cracking and localized damage. Cr and Mo-enriched regions are observed adjacent to the damaged grain boundaries. These elemental distributions are consistent with carbide-containing precipitate regions reported in 316 stainless steels, particularly Cr-rich $M_{23}C_6$ type carbides [53,54]. However, SEM–EDS alone does not provide definitive crystallographic identification; therefore, these features are more appropriately described as Cr and Mo-enriched carbide-containing regions.

The corresponding observations at 725 °C/120 MPa are presented in Fig. 18. Localized GB cracking is visible at low magnification, while higher magnification reveals crack propagation

and damage near precipitate-containing regions. The EDS analysis again indicates local Cr and Mo enrichment. These observations are consistent with GB precipitation and localized creep damage reported for 316/316H stainless steels [53-55].

Taken together, Figs. 16–18 support a progressive damage sequence involving localized GB damage, cavity nucleation, cavity growth, crack development, and final fracture. GB second-phase or precipitate-containing regions can produce local stress and strain concentrations and may facilitate vacancy accumulation and cavity formation during prolonged creep exposure. Continued deformation can promote cavity growth and coalescence, ultimately leading to intergranular crack propagation and rupture [54-57].

The annealing twin boundaries visible in Figs. 17 and 18 should be distinguished from the random or high-angle GB regions where cracking is observed. The present morphological and compositional evidence suggests that localized damage is primarily associated with susceptible GB regions containing or adjacent to second-phase particles rather than with annealing twin boundaries alone. Thus, the failure sequence is best described as a combination of microvoid formation, GB damage, cavity evolution, crack propagation, and final fracture.

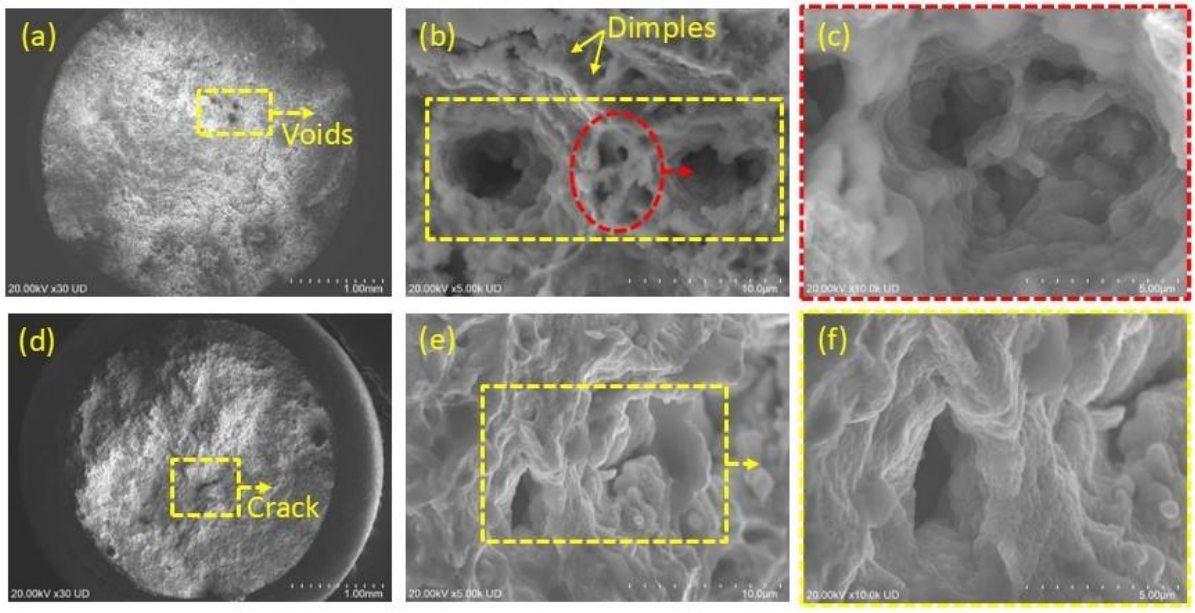
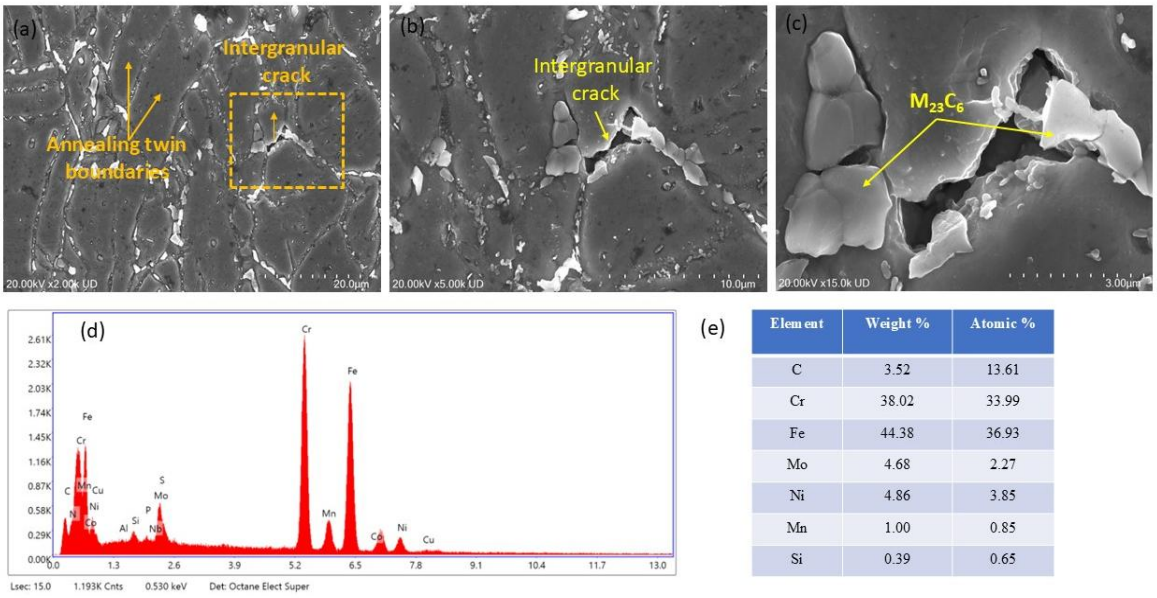
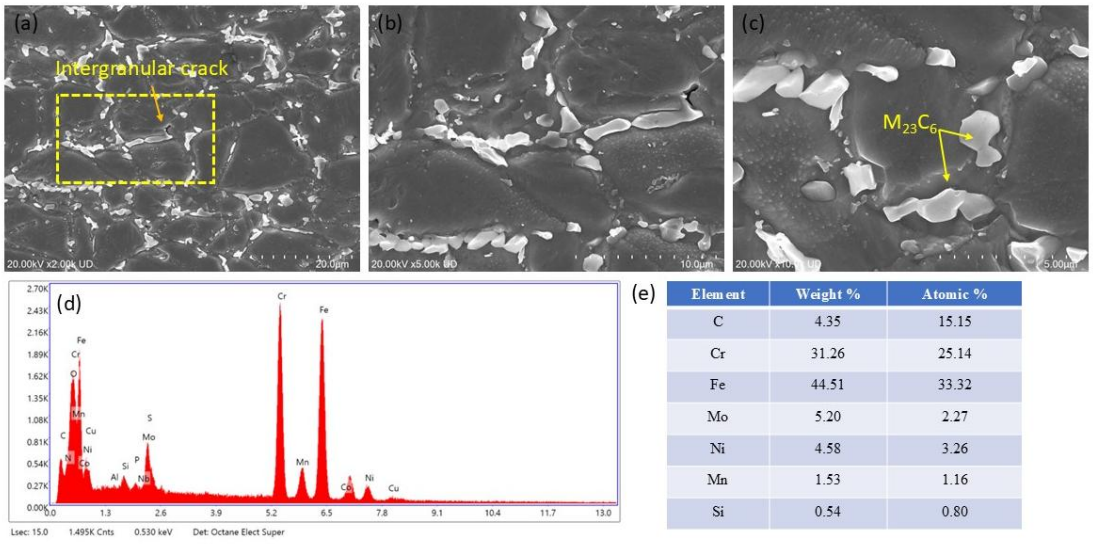


Figure16 SEM fractography of creep tested samples of 316L stainless steel sample tested at 675 ºC/175 MPa (a-c), and at 725 ºC/120 MPa (d-f).



Element	Weight %	Atomic %
C	3.52	13.61
Cr	38.02	33.99
Fe	44.38	36.93
Mo	4.68	2.27
Ni	4.86	3.85
Mn	1.00	0.85
Si	0.39	0.65

Figure 17 SEM microstructure and EDS analysis of 316L stainless steel sample tested at 675ºC/175MPa until ruptured: (a) annealing twin boundaries and intergranular cracking, (b) magnified intergranular crack, (c) grain boundary Cr-rich $M_{23}C_6$ type carbides precipitates associate with crack propagation, (d) EDS spectrum, and (e) corresponding elemental composition.



Element	Weight %	Atomic %
C	4.35	15.15
Cr	31.26	25.14
Fe	44.51	33.32
Mo	5.20	2.27
Ni	4.58	3.26
Mn	1.53	1.16
Si	0.54	0.80

Figure 18 SEM-EDS characterization of creep ruptured sample of 316L stainless steel, tested at 725 °C/120MPa: (a) Intergranular cracking; (b) grain-boundary damage and crack propagation; (c) $M_{23}C_6$ precipitates; (d) EDS spectrum; and (e) elemental composition.

3.10 Prediction Accuracy, Limitations, and overall failure interpretation

The combined results demonstrate that RF, XGBoost, and LightGBM can reproduce the experimentally recorded creep deformation-time response of 316L stainless steel within the investigated temperature, stress, and strain ranges. The stress-specific analyses show that prediction error decreases with increasing applied stress, while the combined-data analysis demonstrates that the models retain high statistical accuracy when both temperatures and all stress conditions are considered.

The conventional creep analysis provides a physical description of the same experimental response. The decrease in stress exponent from 6.9 at 675 °C to 4.5 at 725 °C, the apparent activation energy of approximately 324 kJ mol^{-1}, and the threshold-stress results demonstrate the strong thermomechanical dependence of the deformation process. The Larson-Miller analysis provides an additional empirical correlation, with the strongest relationship obtained for $C = 22$ ($R^2 = 0.990$).

The failure observations provide the microstructural context for the measured creep response. The SEM-EDS and fractographic results indicate that prolonged creep deformation is accompanied by localized grain-boundary damage, carbide-containing regions, cavity formation, crack development, and final fracture. The fracture morphology is predominantly dimpled at 675 °C/175 MPa, whereas the 725 °C/120 MPa condition exhibits more pronounced crack- and cavity-associated features. Because these two representative conditions differ in both temperature and stress, the difference cannot be assigned to temperature alone.

An important limitation of the present ML framework is that the input variables are temperature, applied stress, and measured creep strain. Microstructural descriptors such as grain size, precipitate population, grain-boundary character, and accumulated damage are not explicitly included. Previous studies have shown that incorporating chemical and

microstructural descriptors can improve the representation of creep behavior [58,59]. Consequently, the present model should primarily be applied within the experimental temperature, stress, and deformation domain used for model development.

Another limitation concerns data structure and validation. Multiple observations from a single creep curve are correlated, and the present five-fold cross-validation was performed at the individual data-point level. Therefore, the reported high R^2 values demonstrate strong within-dataset predictive consistency but do not establish fully independent specimen-level generalization. Validation using independent creep curves, additional specimens, or an external experimental dataset would provide stronger evidence for practical deployment.

Finally, the ML predictions should be interpreted as data-driven reproduction of experimentally recorded deformation time rather than as unrestricted prospective prediction of unknown rupture life. Their high statistical accuracy reflects their ability to represent the relationships present in the available experimental dataset. The conventional creep parameters, fractography, and microstructural observations provide the complementary physical basis required for interpreting creep degradation and failure.

4. Conclusion

The high temperature creep behavior and failure characteristics of 316L austenitic stainless steel were investigated experimentally at 675 ºC and 725ºC under multiple applied stresses. An integrated experimental data driven framework combining creep deformation analysis, machine learning prediction, conventional creep kinetics, and post-creep microstructure and fractographic characterization was developed to interpret the temperature and stress-dependent creep response. The main findings are as follows:

- The creep deformation and rupture behavior of 316L stainless steel strongly depended on temperature and applied stress. Higher temperature and stress accelerated creep deformation and reduced rupture time.

- The Norton stress exponent was 6.9 at 675 °C and 4.5 at 725 °C. The apparent creep activation energy was approximately 324 kJ mol^{-1}.
- The Larson-Miller analysis provides a strong correlation at (C = 22), with (R^2 = 0.990). This provides a useful empirical description of rupture behavior within the investigated experimental range.
- RF, XGBoost, and LightGBM reproduced the experimentally recorded deformation time response with high accuracy. For the combined dataset, XGBoost gave the lowest testing error, with (R^2 = 0.9945), RMSE = 9.06 h, and MAE = 4.60 h.
- The ML results represent within-dataset prediction of experimentally recorded deformation time rather than unrestricted prospective rupture-life prediction. The present point-wise cross-validation also does not establish independent specimen-level generalization.
- SEM-EDS and fractography revealed grain-boundary damage, carbide-containing regions, microvoid formation, cavity growth, and crack-associated damage. The fracture morphology varied between the investigated temperature-stress conditions.
- Overall, the combined ML, conventional creep, and post-creep characterization approach provides a quantitative framework for interpreting the deformation and failure behavior of 316L stainless steel.

Acknowledgement

We sincerely thank Binod Kalindi (Senior Technician) and Sumit Kumar Mohanty (AcSIR PhD Scholar) for their valuable guidance and assistance during the experimental creep testing. We express our special thanks to our PhD supervisors, Dr. Ashok Kumar, and Dr. Sunil Kumar for their valuable guidance, encouragement, and motivation throughout the completion of this manuscript.

References

[1]	D. Wen, Z. Li, S. Yue, Y. Li, Q. Wang, B. Jiang, et al., A supersaturated Fe-Cr-Ni super stainless medium-entropy alloy with outstanding structural stability, corrosion resistance, and mechanical properties for elevated-temperature applications, *J. Alloys Compd.* 1055 (2026) 186475.
[2]	B. Li, C. Li, X. Chen, A modified constitutive model for whole-life thermal-mechanical fatigue incorporating dynamic strain aging in 316LN stainless steel, *Mech. Mater.* 197 (2024) 105092.
[3]	D. Kumar, E. Demir, J. Spadotto, B. Connolly, E. Pickering, P. Wilcox, D. Knowles, M. Mostafavi, An integrated CPFE-PCE framework for efficient uncertainty quantification of texture-dependent plasticity in 316L stainless steel, *Mech. Mater.* (2026) 105725.
[4]	Y. Pan, H. Hu, K. Wang, N. Dong, R. Qiu, J.F. Wen, M. Song, S.T. Tu, Creep behavior and fracture mechanism of an additively manufactured 316L stainless steel with extraordinary creep resistance, *Mech. Mater*. 196 (2024) 105053.
[5]	A. Kumar, A. Kumar, S. Kumar, Nanostructure evolution and rupture mechanisms in layered Fe-Cr-Ni alloy under multiaxial tensile deformation: a molecular dynamics study, *J. Mater. Eng. Perform.* 34 (2025) 24542-24555.
[6]	C. Praveen, J. Christopher, V. Ganesan, G.P. Reddy, G. Sasikala, S.K. Albert, Constitutive modelling of transient and steady state creep behaviour of type 316LN austenitic stainless steel, *Mech. Mater.* 137 (2019) 103122.
[7]	V. Romanova, M. Pisarev, D. Lychagin, E. Emelianova, S. Fortuna, V. Mukhin, V. Balokhonov, R. Balokhonov, Multiscale deformation-induced surface pattern in additively manufactured stainless steel under uniaxial tension, *Mech. Mater.* (2026) 105649.

[8]	A. Kumar, A. Kumar, S. Kumar, Defect healing mechanism in Fe-Cr-Ni single crystal under multiaxial cyclic loading: a molecular dynamic simulation-based study, *Fatigue Fract. Eng. Mater. Struct*. (2025) 1-16.
[9]	A. Kumar, S. Kumar, A. Kumar, Atomistic study of mechanical properties of Fe-Cr-Ni alloy under various temperatures and strain rates using molecular dynamics simulation, in: National Conference on Advancement in Materials Processing Technology, 2023, 51-60.
[10]	A. Kumar, R. Kumar, S. Kumar, A. Kumar, Bi-axial deformation induces phase transformation in Fe-Cr-Ni alloys: a molecular dynamics simulation-based study, in: International Conference on Industrial Problems on Machines and Mechanism, 2024, 373–380.
[11]	A. Gokhale, A. Varma, C. Singh, P. Halder, J. Jain, R.K. Yadavalli, Failure analysis of SS 304 HCu reheater tube of a supercritical power plant, *Eng. Fail. Anal.* 137 (2022) 106244.
[12]	Y. Liu, J. Wu, Z. Wang, X.-G. Lu, M. Avdeev, S. Shi, C. Wang, T. Yu, predicting creep rupture life of Ni-based single crystal superalloys using divide-and-conquer approach-based machine learning, *Acta Mater.* 195 (2020) 454-467.
[13]	X. Zhang, J. Yao, Y. Wu, X. Liu, C. Wang, H. Liu, A method for predicting the creep rupture life of small-sample materials based on parametric models and machine learning models, *Materials* 16 (2023) 6804.
[14]	A. Ghatak, P.S. Robi, Modification of Larson-Miller parameter technique for predicting creep life of materials, *Trans. Indian Inst. Met.* 69 (2016) 579-583.
[15]	M.L. Santella, P.F. Tortorelli, M. Render, H. Wang, T. Lach, B.A. Pint, P.J. Maziasz, V. Cedro III, X. Chen, Predicting the creep-rupture lifetime of a cast austenitic

	stainless steel using Larson-Miller and Wilshire parametric approaches, *Int. J. Press. Vessel. Pip.* 205 (2023) 105006.
[16]	M.V. Carneiro, T.T. Salis, G.M. Almeida, A.P. Braga, Prediction of mechanical properties of steel tubes using a machine learning approach, *J. Mater. Eng. Perform.* 30 (2021) 434-443.
[17]	P. Akbari, M. Zamani, A. Mostafaei, Machine learning prediction of mechanical properties in metal additive manufacturing, *Addit. Manuf.* 91 (2024) 104320.
[18]	J. Liu, Y. Zhang, Y. Zhang, S. Kitipornchai, J. Yang, Machine learning assisted prediction of mechanical properties of graphene/aluminium nanocomposite based on molecular dynamics simulation, *Mater. Des.* 213 (2022) 110334.
[19]	V.K. Gupta, N. Kwatra, S. Ray, Artificial neural network modeling of creep behavior in a rotating composite disc, *Eng. Comput.* 24 (2007) 151-164.
[20]	X.C. Zhang, J.G. Gong, F.Z. Xuan, A deep learning-based life prediction method for components under creep, fatigue and creep-fatigue conditions, *Int. J. Fatigue* 148 (2021) 106236.
[21]	L. Breiman, Random forests, *Mach. Learn.* 45 (2001) 5-32.
[22]	T. Chen, C. Guestrin, XGBoost: A scalable tree boosting system, in: *Proceedings of the 22nd ACM SIGKDD International Conference on Knowledge Discovery and Data Mining*, 2016, 785-794.
[23]	J. Chen, X. Liu, L. Zhu, P. Fan, H. Chen, Y. Xie, L. Yue, A study of creep rupture life prediction for P91 steel with machine learning method: model selection and sensitivity analysis, *Int. J. Press. Vessel. Pip.* 216 (2025) 105494.
[24]	J. Xiong, S.Q. Shi, T.Y. Zhang, A machine-learning approach to predicting and understanding the properties of amorphous metallic alloys, *Mater. Des.* 187 (2020) 108378.

[25]	A. Kumar, S. Kumar, A. Kumar, Structural phase transformation in single-crystal Fe-Cr-Ni alloy during creep deformation using molecular dynamics simulation and regression-based machine learning methodology, *Bull. Mater. Sci.* 47 (2024) 7.
[26]	A. Kumar, S. Kumar, A. Kumar, S. Sharma, Prediction of creep degradation in Fe-Cr-Ni single-crystal alloys for high-temperature applications: a molecular-dynamics and machine-learning approach, *Mech. Time-Depend. Mater.* 29 (2025) 8.
[27]	P. Narula, P.A. Kumar, J. Vanaja, G.P. Reddy, G.N. Rao, Machine learning assisted prediction of creep data of India specific reduced activation ferritic martensitic steel, *Mater. Today Commun.* 35 (2023) 106165.
[28]	C. Wang, X. Wei, S. van der Zwaag, Q. Wang, W. Xu, From creep-life prediction to ultra-creep-resistant steel design: an uncertainty-informed machine learning approach, *Acta Mater.* 292 (2025) 121073.
[29]	A. Zare, R.K. Hosseini, A breakthrough in creep lifetime prediction: leveraging machine learning and service data, *Scripta Mater.* 245 (2024) 116037.
[30]	S. Biswas, D. Fernandez Castellanos, M. Zaiser, Prediction of creep failure time using machine learning, *Sci. Rep.* 10 (2020) 16910.
[31]	P. Wang, M. Li, Z. Wen, H. Cheng, Y. Tu, P. He, Machine learning-enabled creep life prediction model for nickel-based single crystal superalloys with consideration of structural shape effects, *Eng. Fract. Mech.* 323 (2025) 111230.
[32]	Brnic, J.,[32 Niu, J., M. Canadija, G. Turkalj, D. Lanc, Behavior of AISI 316L steel subjected to uniaxial state of stress at elevated temperatures, *J. Mater. Sci. Technol.* 25 (2009) 175-180.
[33]	T. Hastie, R. Tibshirani, J. Friedman, *The Elements of Statistical Learning: Data Mining, Inference, and Prediction*, 2nd ed., Springer, New York, 2009.

[34]	G. James, D. Witten, T. Hastie, R. Tibshirani, An Introduction to Statistical Learning: With Applications in R, Springer, New York, 2013.
[35]	H.A. Salman, A. Kalakech, A. Steiti, Random Forest algorithm overview, *Babylonian J. Mach. Learn.* (2024) 69-79.
[36]	W. Su, F. Jiang, C. Shi, D. Wu, L. Liu, S. Li, Y. Yuan, J. Shi, An XGBoost-based knowledge tracing model, *Int. J. Comput. Intell. Syst.* 16 (2023) 13.
[37]	A. Shehadeh, O. Alshboul, R.E. Al Mamlook, O. Hamedat, Machine learning models for predicting the residual value of heavy construction equipment: an evaluation of modified decision tree, LightGBM, and XGBoost regression, *Autom. Constr.* 129 (2021) 103827.
[38]	F.H. Norton, The creep of steel at high temperatures, *McGraw-Hill* Book Company, New York, (1929).
[39]	F.R. Larson, J. Miller, 1952. A time-temperature relationship for rupture and creep stresses, *Transactions of the American Society of Mechanical Engineers* 74(5), (1952) 765-771.
[40]	D. J. Boerman, J. H. Zhu, Study of the accelerated creep fracture process in AISI 316H stainless steel above 800 °C, *Mater. Sci. Eng.* 67(2), (1984), 221-227.
[41]	O. Berk Ozdemir, L. Salvo, E. Ferrie, F. Delabrouille, Creep behavior in austenitic stainless steel 316L(N): effects of minor element additions, *Mater. High Temper.,* 42(1), (2025), 68-77.
[42]	Y. Pan, S.T. Tu, H. Hu, J.-F. Wen, K. Wang, R. Qiu, N. Dong, M. Song, Creep behavior and fracture mechanism of an additively manufactured 316L stainless steel with extraordinary creep resistance, *Mech. Mater.* 196, (2024), 105053.
[43]	Z. Zhang, Z. Gao, H. Tu, X. Wang, X. Mao, J. Wang, D. Diebel, Z. Hu, Three-dimensional characteristic and evolution of creep cavity and microcrack of HR3C

	austenitic heat-resistant steel after long-term creep at 650 °C, *Eng. Fail. Analy.,* 164, (2024), 108634.
[44]	T.G. Langdon, Developments in the creep of materials over a period of more than a century, *J. Mater. Sci.* 60 (2025) 18158-18176.
[45]	C. Herring, Diffusional viscosity of a polycrystalline solid, *J. Appl. Phys.* 21 (1950) 437-445.
[46]	B. Kombaiah, S. Dasari, C. Bhave, S. Shousha, A. Penders, J. Howard, A. Chesetti, N. Mohale, B. Beeler, S. Kadambi, Exploring experimental evidence for diffusional creep mechanisms in alloys, *Microsc. Microanal.* 31 (2025), 48-756.
[47]	Y. Wu, J. Zhang, C. Zhong, J. Liu, K. Hu, X. Lin, Machine learning-assisted creep life prediction and empirical formula generation for 9-12% Cr steel, *Scripta Mater.* 257 (2025) 116480.
[48]	B. Kombaiah, S. Dasari, C. Bhave, N. Mohale, A. Chesetti, S.B. Kadambi, Creep-induced elemental redistribution at grain boundaries of 304L stainless steel-experimental evidence for diffusional creep mechanisms, *Acta Mater.* 294 (2025) 121137.
[49]	S.K. Mohanty, S. Behera, C. Pandey, K. Guguloth, Creep deformation behavior of Grade 91 steel and its weld joints: a comparative study, *Int. J. Press. Vessel. Pip.* 219*,* (2025) 105678.
[50]	J. Weertman, Theory of steady-state creep based on dislocation climb, *J. Appl. Phys.* 28 (1957) 362-364.
[51]	W. Blum, X.H. Zeng, A simple dislocation model of deformation resistance of ultrafine-grained materials explaining Hall-Petch strengthening and enhanced strain rate sensitivity, *Acta Mater*. 57 (2009) 1966-1974.

[52]	M.E. Kassner, T.A. Hayes, Creep cavitation in metals, *Int. J. Plast.* 19 (2003) 1715-1748.
[53]	K.B. Yoon, V.H. Dao, J.M. Yu, Effects of build direction on tensile and creep properties of 316L stainless steel produced by selective laser melting, *Fatigue Fract. Eng. Mater. Struct.* 43 (2020) 2623-2636.
[54]	T.L. Burnett, R. Geurts, H. Jazaeri, S.M. Northover, S.A. McDonald, S.J. Haigh, P.J. Bouchard, P.J. Withers, Multiscale 3D analysis of creep cavities in AISI type 316 stainless steels, *Mater. Sci. Technol.* 31 (2015) 522-534.
[55]	B. Chen, P.E.J. Flewitt, D.J. Smith, C.P. Jones, An improved method to identify grain boundary creep cavitation in 316H austenitic stainless steel, *Ultramicroscopy* 111 (2011) 309-313.
[56]	S. He, H. Shang, A. Fernández-Caballero, A.D. Warren, D.M. Knowles, P.E.J. Flewitt, T.L. Martin, The role of grain boundary ferrite evolution and thermal aging on creep cavitation of type 316H austenitic stainless steel, *Mater. Sci. Eng. A* 807 (2021) 140859.
[57]	N. Shinya, H. Tanaka, M. Murata, M. Kaise, S. Yokoi, Creep fracture mechanism maps based on creep rupture tests up to about 100 000 h for type 316 stainless steel, Tetsu-to-Hagane 71 (1985) 114-120.
[58]	L. Wei, S. Wang, W. Hao, J. Huang, N. Qu, Y. Liu, J. Zhu, Prediction of high-temperature creep life of austenitic heat-resistant steels based on data fusion, *Metals* 13 (2023) 1630.
[59]	H.K. Bhardwaj, M. Shukla, Machine learning-based improved creep life prediction of 316 austenitic stainless steel with add-on chemical and microstructural features, *J. Mater. Eng. Perform.* 34 (2025) 18978-18996.